TEKTONIKA

Signatures of Fluid-Rock Interactions in Shallow Parts of the San Andreas and San Gabriel Faults, Southern California

James P. Evans *[1], **Kaitlyn A. Crouch** [1,2], **Caroline Studnicky**[1,3], **Sharon Bone** [4], **Nicholas Edwards** [4], **Samuel M. Webb** [4]

[1]Department of Geosciences, Utah State University, Logan, UT 84322-4505, USA | [2]Now at: Department of Geosciences, University of Wisconsin, Lewis G. Weeks Hall, 1215 West Dayton Street, Madison, WI 53706-1692, USA | [3]now at: Chevron North America Exploration and Production, 6301 Deauville Boulevard Midland, TX 79706, USA | [4]Stanford Synchrotron Radiation Lightsource, SLAC National Accelerator Laboratory 2575 Sand Hill Road, MS 69 Menlo Park, CA 9402, USA

Abstract We examine deformed crystalline bedrock in the upper parts of the active San Andreas and ancient San Gabriel Faults, southern California, to 1) determine the nature and origin of micro-scale composition and geochemistry of fault-related rocks, 2) constrain the extent of fluid-rock interactions, and 3) determine the interactions between alteration, mineralization, and deformation. We used drill cores from a 470 m long inclined borehole through the steep-dipping San Gabriel Fault and from seven inclined northeast-plunging boreholes across the San Andreas Fault zone to 150 m deep to show that narrow fault cores 10 cm to 5 m wide lie within 100s m wide damage zones. Petrographic, mineralogic, whole-rock geochemical analyses and synchrotron-based X-ray fluorescence mapping of drill core and thin sections of rocks from the damage zone and narrow principal slip surfaces reveal evidence for the development of early fracture networks, with iron and other transition element mineralization and alteration along the fractures. Alteration includes clay ± chlorite development, carbonate, and zeolite mineralization in matrix and fractures and the mobility of trace and transition elements. Carbonate-zeolite mineralization filled fractures and are associated with element mobility through the crystalline rocks. Textural evidence for repeated shearing, alteration, vein formation, brittle deformation, fault slip, pressure solution, and faulted rock re-lithification indicates significant hydrothermal alteration occurred during shallow-level deformation in the fault zones. The rock assemblages show that hydrothermal conditions in active faults develop at very shallow levels where seismic energy, heat, and fluids are focused.

Executive Editor:
Craig Magee
Associate Editor:
Noah Phillips
Technical Editor:
Mohamed Gouiza

Reviewers:
Lydia Baily
Tsuyoshi Ishikawa
Simone Masoch

Submitted:
31 May 2023
Accepted:
22 May 2024
Published:
19 August 2024

1 Introduction

The upper 2-5 km of seismogenic faults exhibit coseismic slip deficits (*Kaneko and Fialko*, 2011; *Xu et al.*, 2016), adsorb energy (*Shipton et al.*, 2006; *Zhao et al.*, 2024), and do not nucleate seismic slip nor radiate seismic energy (*Scholz*, 2019; *Xu et al.*, 2016). Yet, long-term slip and deformation must occur in shallow parts of fault zones for crustal strains to be compatible over the entire depth range of a fault (*Rice and Tse*, 1986; *Marone and Scholz*, 1988). Maximum values of coseismic slip on continental strike-slip faults typically occur at depths > 3 km (*Marone and Saffer*, 2007; *Kaneko and Fialko*, 2011; *Dolan and Haravitch*, 2014; *Scott et al.*, 2019), although these interpretations depend on the nature of the inversion scheme and the assumptions made regarding the structure of faults (*Marchandon et al.*, 2021). Seismic slip maxima at depths of 4 to 10+ km diminishes to ~50% of these maxima towards the Earth's surface as revealed in earthquake foci (*Hauksson and Meier*, 2019) and coseismic slip or geodetic inversions of Mb> 7.0 strike-slip faults (*Archuleta*, 1984; *Kaneko and Fialko*, 2011; *Dolan and Haravitch*, 2014; *Scott et al.*, 2019; *Xu et al.*, 2016).

Mechanisms to explain shallow slip deficits include frictional slip on weak fault-related rocks, pore-fluid pressure weakening (*Marone and Saffer*, 2007), bulk plastic yielding, and other anelastic processes (*Roten et al.*, 2017; *Scott et al.*, 2019). Many inversion schemes do not include off-fault distributed deformation (*Scott et al.*, 2019; *Marchandon et al.*, 2021), whilst compliant fault zones (*Cochran et al.*, 2009; *Kaneko and Fialko*, 2011; *Xu et al.*, 2016) composed of low cohesive and frictional strength rocks (*Boulton et al.*, 2017; *Chester et al.*, 1993; *Isaacs et al.*, 2008; *Jeppson et al.*, 2010; *Bradbury et al.*, 2011; *Jeppson and Tobin*, 2015) perhaps altered by hydrothermal fluids, may enable slip and coseismic

*✉ james.evans@usu.edu

energy to be consumed within low-elastic moduli fault damage zone rocks.

The composition, textures, and fine-scale morphology of fault-related rocks record evidence for chemical and physical processes within fault zones (*Chester et al.*, 1993; *Rowe and Griffith*, 2015; *Faulkner et al.*, 2003, 2010; *Smith et al.*, 2013; *Townend*, 2017; *Boulton et al.*, 2017). Clay ± chlorite ± phyllosilicate-rich fault zones in exhumed fault zones (*Chester et al.*, 1993; *Faulkner et al.*, 2010; *Moore and Rymer*, 2012; *Schulz and Evans*, 1998; *Bradbury et al.*, 2015; *Mitchell and Faulkner*, 2009; *Moser et al.*, 2017) and in the deep 2.7 km core (*Gratier et al.*, 2011; *Bradbury et al.*, 2015; *Holdsworth et al.*, 2011; *Richard et al.*, 2014; *Schleicher et al.*, 2009) provide evidence for the chemical and mechanical processes operating at shallow crustal levels. Alteration driven by heat and fluids in fault zones and advective fluid flow may explain the presence of veins, clay-rich fault gouge, alteration assemblages such as hydrologically driven alteration of hornblende to iron-oxides ± chlorites or feldspars to clay, mineralization within faults, and pressure solution. These features likely form at hydrothermal conditions—at temperatures above the background geothermal conditions (*Bruhn et al.*, 1994; *Callahan et al.*, 2020; *Dorsey et al.*, 2021).

The previous work on fault zone composition and recent work on shallow fault-slip deficits begs several questions: 1) What is the composition and structure of the shallowest parts of the bedrock (not unconsolidated deposits) component of faults (*Nevitt et al.*, 2020)? 2) What is the nature and extent of alteration, mineralization, and other fluid-rock interactions in the shallow parts of fault zones? and 3) What are the processes responsible for these transformations? Addressing these questions requires examining deformation in the shallow parts of faults at various scales using various methods.

Chemical and mineralogic characterizations of deformed rocks are fundamental to determining the composition of these rocks, which then informs models of rock properties and their changes over the history of the sheared rocks (*Niemeijer et al.*, 2016; *Faulkner et al.*, 2010; *Mitchell and Faulkner*, 2009). Variations in major-, minor-, and, in many cases, trace-element distribution and concentrations provide valuable insights into the nature and degree of fluid-rock / hydrothermal processes in faults and determine the elemental and mineral composition and distribution that influence the mechanical behavior and textures of these sheared rocks.

2 Objectives

We use multi-scale and multimodal approaches to examine the extent and nature of deformation and alteration in the upper part of active fault zones at shallow crustal levels. We use the results of recent studies and present new data on drill core samples retrieved from the upper 400 m of the active San Andreas and ancient San Gabriel fault zones to examine fault-related composition and determine the nature of alteration and mineralization in the fault zones. *Crouch and Evans* (2023), *Studnicky* (2021), and *Williams et al.* (2021) document the nature of fault zone deformation mechanisms, mineralogy, and micro-to-mesoscopic structures of these fault-related rocks. Samples and borehole-based data from continuously cored boreholes provide samples of all fault zones, and the rocks have well-preserved deformation and altered textures with slight to no surface-related alteration.

We use optical and scanning electron microscopy, standard whole-rock geochemical analyses, and X-ray synchrotron radiation-sourced scanning X-ray fluorescence (SRS-XRF) mapping (*Bergmann et al.*, 2020; *Edwards et al.*, 2018) to 1) determine elemental compositions and their variations in deformed rocks at μm to 10's cm scales, 2) constrain the nature of fluid-rock interactions in very shallow parts of seismogenic faults, and 3) show the utility of integrating microscale chemical maps and analyses with traditional geochemical analyses, and textural studies at the outcrop, drill-core, and thin-section m-scales scales to examine the nature of fault-related rocks.

3 Geologic Setting and Samples

We examine two suites of samples acquired in recent geotechnical drilling studies across the active San Andreas and the ancient San Gabriel Faults in southern California. The San Andreas Fault (SAF) system accommodates most transform plate motion between the Pacific and North American Plates in southern California (Irwin, 1990). In the Mojave region, slip on the Punchbowl and San Gabriel Faults (SGF) (*Powell and Weldon*, 1992; *Powell*, 1993; *Nourse*, 2002) preceded the active San Andreas Fault (Figure 1).

The active San Andreas Fault at the Elizabeth Lake study site is expressed as an ∼450-m wide linear valley (*Wallace*, 1949; *Dibblee and Carter*, 2002; *Hernandez*, 2011) where 10-30 m thick sequences of Quaternary deposits are cut by active traces of the San Andreas Fault (*Ross*, 1984; *Bemis et al.*, 2021). The underlying bedrock at the site (*Dibblee and Carter*, 2002; *Hernandez*, 2011; *LADWP*, 2019) is composed of Precambrian quartzo-feldspathic and amphibolite gneiss on the southwest (Pacific Plate) side of the fault and Cretaceous granitic to quartz diorite, and Mesozoic and older Pelona Schist on the northeast (North American) side of the fault (Figure 1). The geotechnical investigations at the Elizabeth Lake study site consist of seven northeast-plunging boreholes along a 011° trending, 210-m long transect drilled by the Los Angeles Department of Water and Power (*LADWP*, 2019; *Williams et al.*, 2021) to depths of 144 m across the San Andreas Fault (Figures 1 and 2a). The Los Angeles Aqueduct crosses the fault at 900 m elevation,

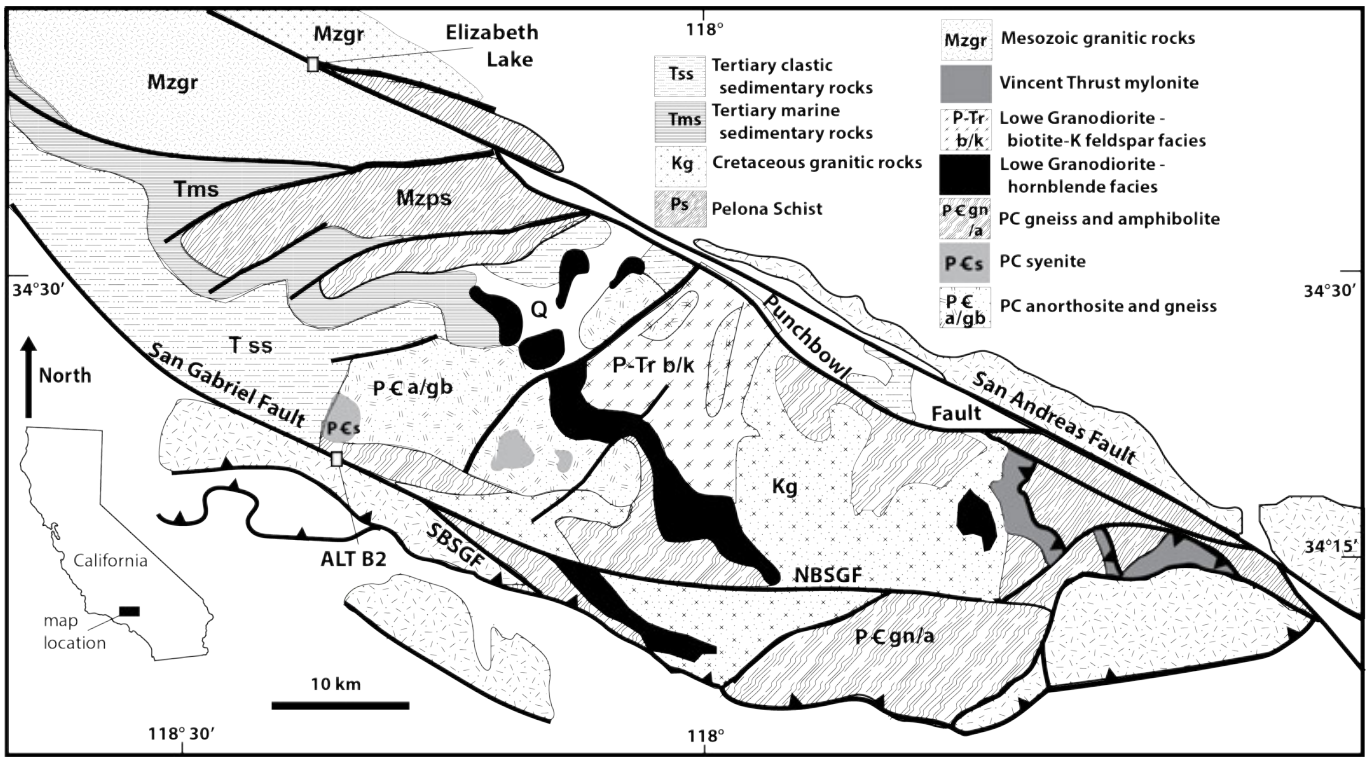

Figure 1 – General fault map of southern California of the San Gabriel Mountains, CA, adapted from *Yerkes and Campbell* (2005) and *Nourse* (2002). Bold lines represent faults from the SCEC CFM5.3 database. The San Gabriel Mountains consist of a sequence of crystalline and sedimentary rocks uplifted by recent and active, south-directed thrusting, which has exhumed ancient faults that cut the basement rocks. The locations of the Lake Elizabeth transect across the San Andreas Fault and the ALT-B2 borehole across the San Gabriel Fault are indicated.

~100 m below the ground surface (*Mulholland*, 1918; *Sutherland et al.*, 2013).

The Mojave segment of the SAF last ruptured in the 1857 magnitude 7.8 Fort Tejon earthquake (*Zielke et al.*, 2010) and accommodates 22 to 28 mm/yr of slip with an average of 4 m/event of horizontal displacement (*Scharer and Streig*, 2019). The Elizabeth Lake site lies at the transition of the fault segment's Mojave North and South sections (*Field et al.*, 2014). It is an essential site for determining the paleoseismic records of the San Andreas Fault in the region (*Bemis et al.*, 2021). Mesoscopic description of the drill core and geophysical logs of the boreholes (*LADWP*, 2019), interpretation of the as-built logs of the aqueduct (*Mulholland*, 1918; *Sutherland et al.*, 2013), and analyses of the drill core (*Lindvall et al.*, 2018; *Studnicky*, 2021; *Williams et al.*, 2021) indicate that the inner part of the fault zone consists of an up to 400-m wide fault damage zone within a 1-km wide fault zone, with several principal slip surfaces that may have experienced ~15 cm of aseismic(?) slip in the past 100 years (*Tayyebi et al.*, 2017). Regional exhumation was ~2 km (*Buscher and Spotila*, 2007) in the past 10 Myr. Within this fault zone, several zones of highly sheared, foliated slip zones 10 cm to 2 m wide appear to be the loci of most of the slip (*Mulholland*, 1918; *Sutherland et al.*, 2013; *LADWP*, 2019; *Williams et al.*, 2021; *Studnicky*, 2021) and these may project to the surface where Quaternary offsets are observed (*Scharer and Streig*, 2019; *Bemis et al.*, 2021, Figure 2).

The San Gabriel Fault exhumed in the San Gabriel Mountains (Figure 1), is exposed in bedrock at the surface (*Anderson et al.*, 1983; *Chester et al.*, 1993; *Evans and Chester*, 1995) and is sampled by an ~60°-plunging, 493 m-deep borehole (Figure 2b) that intersects the western San Gabriel Fault shear zones at 313 and 420 m deep (*Crouch and Evans*, 2023). This hole was drilled for geotechnical investigations by the California High-Speed Rail system and provides a range of data that we use to decipher the elastic and seismic properties of the fault (*Crouch and Evans*, 2023).

The Precambrian Mendenhall Gneiss is the protolith on the north side of the San Gabriel Fault, which consists of felsic gneiss and mafic granulite. On the south side, the protolith lithologies are Mesozoic quartz diorite, granite, tonalite, and quartz-diorite gneiss. The San Gabriel Fault accommodated up to 42 km of transform slip between 13 and 5 Ma (*Powell*, 1993; *Nourse*, 2002), and as much as 5 km of post-Miocene slip may have occurred along parts of the San Gabriel and Vasquez Faults (*Beyer et al.*, 2009; *Bryant and Compiler*, 2017). The San Gabriel Mountains have been uplifted due to south-directed slip on the underlying north-dipping Sierra Madre thrust fault, and the rocks related to ancient slip on the SGF are exhumed from 2 to 5 km depths (*Chester et al.*, 1993; *Spotila et al.*, 2002; *Blythe et al.*, 2002) to reveal a narrow fault core along which most of the fault slip occurred within a damage zone (*Chester et al.*, 1993; *Evans and Chester*, 1995;

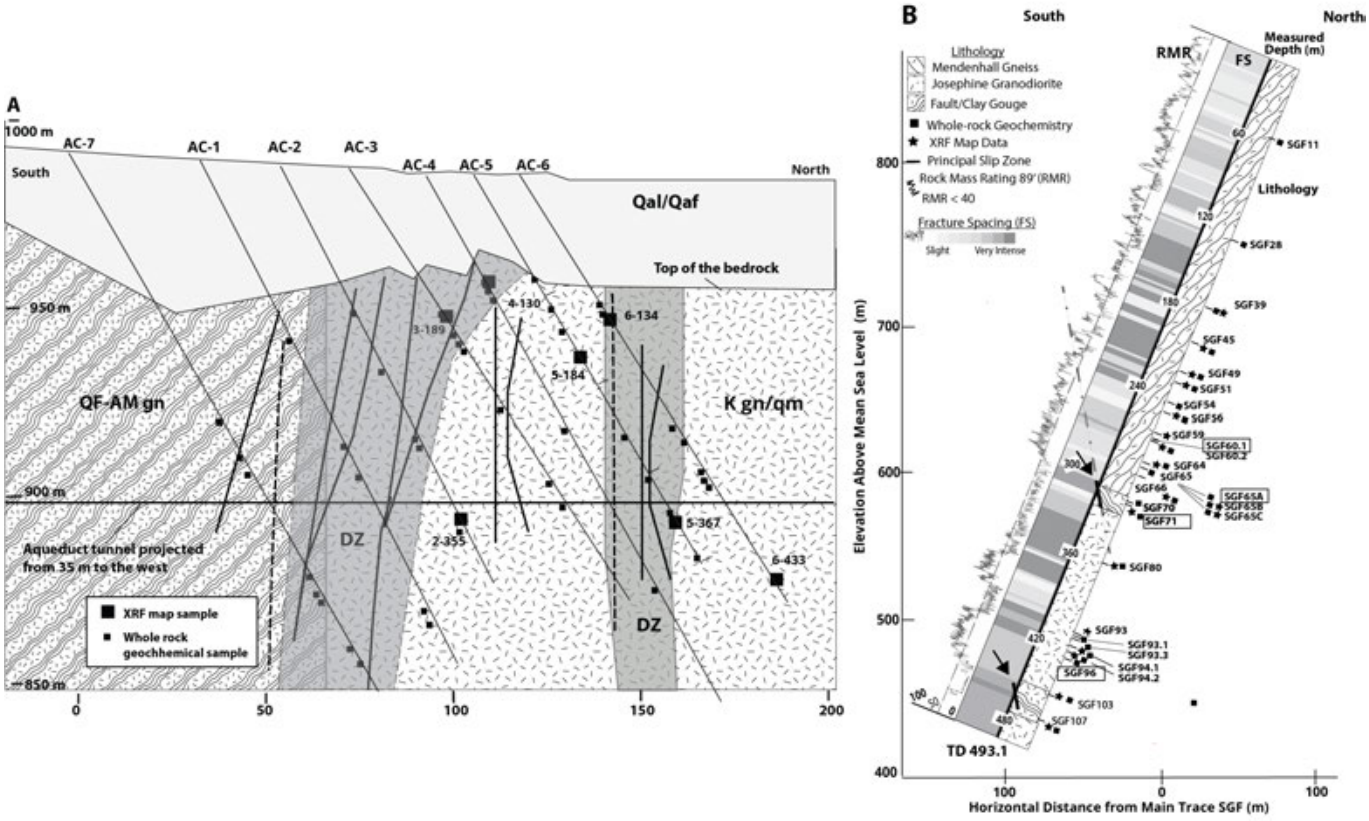

Figure 2 – Simplified geology cross-sections of the study areas. **A)** Cross section of inferred fault structure and associated damage zones of the San Andreas Fault at the Elizabeth Lake site, with the locations of the boreholes and samples shown. Modified from *LADWP* (2019); *Studnicky* (2021); *Williams et al.* (2021). The simplified geology of the drill site shows damage zones (DZ) in dark gray shading, interpreted from core logs and resistivity logs, are 20-60 m thick and contain narrow slip surfaces indicated by the bold black lines that are defined by the presence of cataclasite and ultracataclasite in the core. Rocks southwest of the fault zone (Pacific side) consist of quartzo-feldspathic and amphibolite gneiss (QF-Am gn). On the North American side, rocks to the northeast are Cretaceous granodiorite-to-quartz monzonites (K Gn-qm). Shallow auger boreholes and cone penetrometer tests in the Quaternary sediments indicate the presence of two 5-7 m high steps in the contact between the bedrock and the Quaternary deposits (Qal and Qaf), which are aligned with the active trace of the fault from the work of *Scharer and Streig* (2019); *Bemis et al.* (2021). Descriptions of the fault zone made during tunnel construction (*Mulholland*, 1918) indicate the presence of flowing water, clay-rich fault gouge, and mineralized zones that correspond to the location of the fault zones at the tunnel level shown here. **B)** Simplified cross section of the ALT-B2 borehole adapted from *Crouch and Evans* (2023). The ALT-B2 borehole plunges 68° south through the SGF to a total measured depth of 493.1 m. Simplified lithology, fracture density, locations of core samples, geochemical data, rock mass rating (RMR) values, and the locations of the fault zone are shown. The lithologies of rock intersected by the borehole consist of Mendenhall Gneiss to 313 m depth and Josephine Granodiorite to the bottom. The ALT-B2 borehole intersected two principal slip zones, two damage zones, highly fractured zones, and two zones of lower fracture intensity and plastic shear. The fracture spacing is at least one fracture every: slight=30-90 cm; moderate=10-30 cm; intense 2.5-10 cm; very intense <2.5 cm.

d'Alessio et al., 2003; *Crouch and Evans*, 2023). The drill core extends to depths of 493 m and forms a shallow angle with the steeply dipping San Gabriel Fault (Figure 2b], thereby sampling a large portion of the fault damage zone with little interference from near-surface alteration. Fault-related rocks from the SGF thus likely formed at 2.5-5.5 km depth.

4 Methods

Core-based studies of fault zones provide access to deformed rocks that experienced less surface-related weathering and alteration, which enables us to examine rocks with well-preserved deformation-related alteration and deformation textures (*Boulton et al.*, 2017; *Bradbury et al.*, 2011; *Duan et al.*, 2016). The mesoscopic analyses of the drill core, microstructural analyses of deformed rocks, and mineralogy from X-ray diffraction studies for these boreholes (*Studnicky*, 2021; *Williams et al.*, 2021; *Crouch and Evans*, 2023) guide the analyses of the microchemistry with synchrotron radiation-based studies. Details of how the drill core was acquired are in *Crouch and Evans* (2023); *Studnicky* (2021); *Williams et al.* (2021); *LADWP* (2019).

Whole-rock geochemistry major-, minor-, trace-, and rare-earth element analyses were performed on 46 samples from the Lake Elizabeth samples and 41 drill core samples and nine outcrop samples from the San Gabriel Fault by ALS Geochemistry Labs using X-ray fluorescence, Inductively Coupled Plasma Atomic Emission Spectroscopy (ICP-AES), and

Inductively Coupled Plasma Mass Spectrometry (ICP-MS) analyses on ~2 g aliquots. For the San Gabriel Fault site, we compare our data on deformed rocks with the protolith whole-rock geochemistry data of *Anderson et al.* (1983), *Barth et al.* (1995a,b), and *Evans and Chester* (1995). For the Lake Elizabeth site, we compare the whole-rock data from quarto-feldspathic protolith geochemical analyses from our work, *Ross* (1984) and *Wechsler et al.* (2011). We use covariance analyses with 95% probability (*Williams et al.*, 2021) to statistically estimate likely groupings of the rock types and their variations within the fault zone. *Crouch and Evans* (2023) and *Studnicky* (2021) examined the deformation microstructures and textures with optical and, secondary, and back-scattered electron microscopy and X-ray diffraction mineralogical analyses to constrain mesoscopic deformation textures and inferred processes from the shallow parts of the faults.

We mapped the distribution and relative concentrations of elements at the μm scale in samples of deformed rocks with scanning X-ray fluorescence (SRS-XRF) at the Stanford Synchrotron Radiation Laboratory (SSRL). The data set includes 22 samples with 52 elemental map regions from the San Gabriel Fault and 17 samples with 48 maps from the Lake Elizabeth site. The incident beam energy, spot size, and dwell times are consistent for all the analyses. The SRS-XRF enables rapid elemental concentration analyses across the same map areas as viewed in thin sections. For details of the analytical methods and settings for the micro-XRF mapping and XAS analyses, see Supporting Information.

Synchrotron-based analyses (*Kelly et al.*, 2008; *Renard et al.*, 2016; *Bergmann et al.*, 2020) have examined a range of archeologic, artistic, geologic, and palaeontologic materials but have seen relatively little use in the low- to moderate temperature-pressure geologic deformation realm (*Fusseis et al.*, 2014; *Farfan et al.*, 2018). We use techniques these workers developed and new developments (*Edwards et al.*, 2018) to examine the altered and deformed fault-related rocks with X-ray fluorescence mapping to determine high-resolution analyses of composition and textures. The XRF mapping requires little to no sample preparation or polishing, and the X-ray interacts with a very thin surface; thus, non-destructive analyses of small, rare, and delicate samples with little electron interaction below the surface are relatively straightforward. The studies are done at ambient temperatures and pressures, so no vacuum pressures or degassing issues affect detector performance. These advantages enable us to determine the relationships between elemental concentrations and deformation fabrics that we cannot decipher at the whole-rock geochemical scale.

Samples were analyzed on beamlines 2-3, 10-2 (now 7-2), and 6-2 at the SSRL (See Appendix 1 for details). The method focuses a beam of high-energy X-rays as small as 2 μm on a sample that excites inner shell electrons, which are ejected from the sample at or above their binding energies. Filling this vacancy with outer shell electrons emits a specific fluorescent energy unique to each element. By illuminating a sample at or above the excitation energy of the electron's binding energy and moving the sample under a stational X-ray beam, we rapidly map the distribution of the elements (*Edwards et al.*, 2018). The sample holders, beamline configurations, and data acquisition software at SSRL enable us to characterize standard 2 x 3 cm and 5 x 7.5 cm thin sections and a 60-80 cm long piece of core. Low-resolution rapid scans at 10-50 m spot sizes determine the general character of the elemental distributions. Subsequent high-resolution analyses at 2-5 μm spot sizes at similar beam conditions generate detailed maps of the element distribution of the deformed samples. We examine samples with the same analytical conditions at 10^{-6} to 10^{-1} μm-scales. Data for up to 16 elements are collected for rapid data interrogation at the beamline, and the full XRF spectrum per pixel dataset is collected concurrently for more time-consuming post-experiment in-depth interrogation of the data.

4.1 Distribution of Metals in Fault-Related Rocks

Many rocks examined consist of dark to optically opaque mm- to cm-thick aphanitic brown and black material (e.g., *Chester et al.*, 1993), typically cataclasites, ultracataclasite, fine-grained fault gouge enriched in Fe, Mg, and Mn (*Anderson et al.*, 1983; *Evans and Chester*, 1995; *Crouch and Evans*, 2023; *Williams et al.*, 2021). Whole-rock geochemical analyses in conjunction with optical or scanning-electron microscopy are standard methods to evaluate compositional variations in fault-related rocks. These have limitations owing to the sample distribution and size, especially relative to the micron-scale variations in elemental concentrations. We collected synchrotron X-ray data at 2 – 25 μm scales in thin sections and 10-50 μm for core samples at the Fe Kα 7100 eV edge for elements between S and Zn, with particular focus on Ca, Ti, V, Cr, Mn, Fe, Ni, and in some cases, Zn and K. These elements exhibit variations in whole-rock chemical data associated with textures of the faulted and altered rocks of the San Andreas and San Gabriel faults (*Evans and Chester*, 1995; *Bradbury et al.*, 2015; *Williams et al.*, 2021; *Crouch and Evans*, 2023). These elements have a range of reduction potentials and solubilities in fluids, resulting in diverse geochemical behaviors depending on the fluid composition, pO_2 values of the fault environment, and temperatures. They are among the most abundant minor- and trace elements in the upper crust, and transition metals can form a range of oxides and sulfides in hydrothermal and altered rocks. Iron, manganese, and other metals are often concentrated in faults

and shear zones (*O'Hara*, 1992; *Evans and Chester*, 1995) and can be used to examine the nature and timing of fluid-rock interactions in deformed rocks (*Cooperdock and Ault*, 2020).

5 Results

5.1 Mesoscopic Fault Structure

The inner, most highly deformed portion of the San Andreas Fault zone at Elizabeth Lake is a ~300-400 m wide damage zone determined from core logging (Figure 2a; *Studnicky*, 2021; *LADWP*, 2019; *Williams et al.*, 2021), wireline geophysical log data from the LADWP project, the as-built data for the aqueduct (*Mulholland*, 1918; *Sutherland et al.*, 2013), and fault-rock analyses (*Williams et al.*, 2021; *Studnicky*, 2021). The entire fault zone is likely over 1 km wide (*Mulholland*, 1918; *Wallace*, 1949), and the rocks examined here come from the inner, highly deformed part of the fault zone (*LADWP*, 2019; *Williams et al.*, 2021). The likely central fault zone dips steeply south (Figure 2a). It is expressed as several 5-10 cm thick zones of ultracataclasites within fractured, faulted, and chloritically altered clay-rich slip zones within the damage zone rocks (Figure 3). At the top of the bedrock, cone penetrometer data indicate the location of two fault strands (Figure 3) that offset the contact between the bedrock and unconsolidated sediment. These active traces are extrapolated downdip into the core and are expressed as zones of dark brown, green, and black cataclasites in highly deformed and altered rocks (*Williams et al.*, 2021; *Studnicky*, 2021) that are moderately to highly indurated in the cored sections. Highly deformed clay-rich faults (*Williams et al.*, 2021) are interspersed with less deformed cataclasites and damage zone rocks, and all rocks in the drill core exhibit some level of damage (*Studnicky*, 2021). These zones consist of chlorite ± calcite ± epidote ± clay shear zones, cataclasites, and altered rock regions that include calcite, zeolites, chlorite, and Fe-oxides. Sharp boundaries define fault slip zones, and clasts of earlier-formed cataclasite are present (Figure 3).

At depth in the San Gabriel borehole, the fault core is as much as 1-3 m thick within a 170-m wide damage zone (*Crouch and Evans*, 2023). Medium-foliated protolith gneiss gives way to indurated, chlorite-deformed quartzofeldspathic altered host rock and shear zones (Figures 2b and 4). Rocks near the central fault zone are chloritic breccia, cataclasites, and foliated cataclasites (Figures 2b and 4 *Crouch*, 2022; *Crouch and Evans*, 2023). Rocks from the San Gabriel Fault (Figure 4) range from protolith and sheared chloritic breccia (Figure 4a) to thin ultracataclasite and cataclasite (Figure 4b). Rocks in the southwestern damage zone consist of foliated shear rocks with calcite veins and zeolite layers (Figure 4c) and highly sheared, extremely fine-grained foliated cataclasites and phyllonites (Figure 4d, e). In field exposures, the San Gabriel Fault core is 1-10 cm wide (*Anderson et al.*, 1983; *d'Alessio et al.*, 2003; *Chester et al.*, 1993; *Chester and Chester*, 1998; *Evans and Chester*, 1995; *Crouch and Evans*, 2023) within adjacent intensely deformed zones 5-10 m wide, and a~100 m thick damage zone.

The detailed descriptions of the microscopic-scale deformation and alteration textures of rocks from the two sites (*Crouch and Evans*, 2023; *Studnicky*, 2021; *Williams et al.*, 2021) provide the context for the geochemical and XRF- analyses presented in this paper. Optical petrography and X-ray diffraction analyses show that the protolith gneiss is moderately to highly altered within the fault damage zones. In the San Andreas Fault (Figure 5) the common alteration assemblages are calcite, zeolites (primarily laumontite, wairakite, and heulandite), chlorite, smectite, hematite, and epidote (*Williams et al.*, 2021; *Studnicky*, 2021). Fault-related rocks from the San Andreas Fault exhibit microbreccias, cataclasites, ultracataclasites, deformed carbonates, and zeolites (Figure 5). Repeated brittle deformation in the San Andreas fault zone is recorded by the presence of clasts of subrounded breccia that lie within other breccias (Figure 5A, B), which are in turn cut by sheared cataclasites which with clast of earlier formed breccias (Figure 5B). Clasts of zeolite-rich fragments lie within cataclasites (Figure 5B), and calcite cements between these two dominant fault-related textures (Figure 5A, B), indicating that faults cut early zeolite zones and carbonate cementation occurred along the edges of cataclasites. Narrow shear zones cut quartz-feldspar-rich gneiss and sheared and altered breccias contain elongate, irregular zones of phyllosilicates and calcite clasts (Figure 5C, D). The fault-related rocks at the Lake Elizabeth site also contain pulverized rocks (*Dor et al.*, 2006; *Ostermeijer et al.*, 2022). Pulverized rocks have networks of intragranular fractures, some filled with injection breccias that formed in adjacent cataclasites (Figure 5E, F). Clasts of crushed rocks are entrained in the cataclasite, and breccias and altered host rocks are cut by cataclasite-filled fractures that emanate from the cataclasite (Figure 5F).

Samples from the San Gabriel fault indicate the effects of distributed shearing, alteration, and mineralization (*Crouch and Evans*, 2023, (Figure 6)). The host rock here consists of quartz, albite, anorthite, and muscovite. In the damage zone, smectite, phlogopite, calcite, and undifferentiated zeolites are present. Ti- and Mn-oxides, epidote, and clinochlore appear throughout the damage zone in the highly sheared rocks. These minerals are sheared, occupy fractures, and replace feldspars, amphiboles, or biotite (*Crouch and Evans*, 2023).

Rocks from the damage zone of the upper fault zone (see Figure 2B) are comprised of brittly deformed and altered gneissic protolith cut by cm-thick shear zones. Evidence for multiple phases of alteration, shearing, and folding are marked by

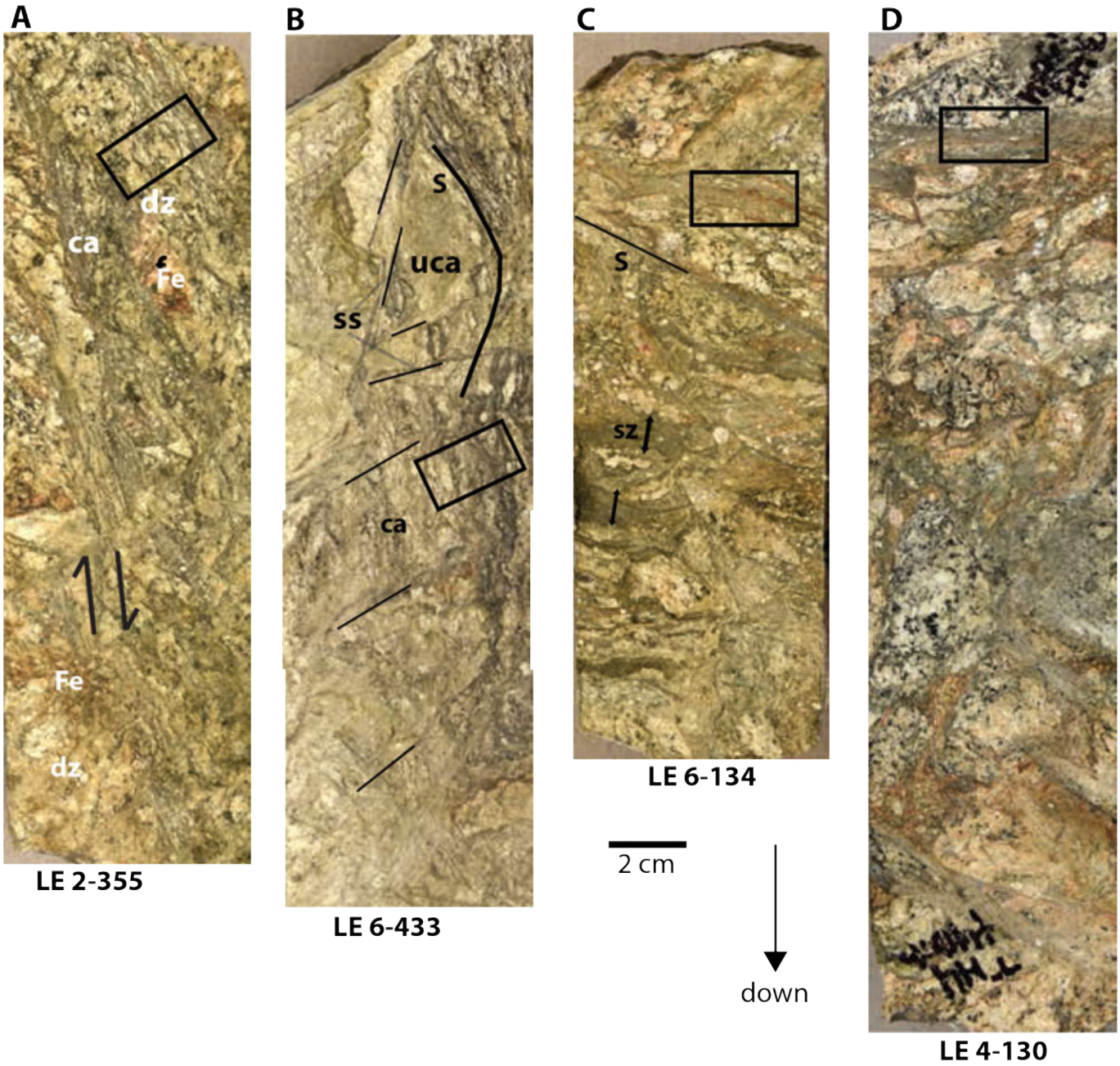

Figure 3 – Photographs of the Lake Elizabeth core sections across the San Andreas Fault representing the deformation and alteration textures were examined with XRF mapping. Boxes indicate the locations of the. XRF map samples. **A)** Sample LE 2-355 is from the deformed rocks north and below of the damage zone associated with the southern, and likely primary, fault zone. The sheared chlorite-rich zones at shallow core-foliation angles (arrows indicate the orientations of the foliated zones) consist of deformed damage zone rocks (dz), thin cataclasite (ca), and feldspars (f). Rounded white zones are remnant feldspar-rich fragments in highly deformed protolith with little primary structure visible. Zones of iron oxides (Fe) lie next to cataclasite zones. The black box indicates the area mapped with the XRF analyses. **B)** Sample 6-433 from the deepest part of the North American side of the fault. Ultracataclasite (uca) and cataclasite (ca) are cut by narrow slip surfaces (ss) indicated by the medium thickness at high to moderate angles to within highly sheared, foliated host rocks with irregular foliation (s) and clasts of deformed protolith. Note the subvertical wavy foliation of the chlorite-rich cataclasite. **C)** Sample LE 6-134, from within or within a fault zone on the northern side of the fault zone. Narrow slip surfaces (s) and shear zones (sz) are nearly perpendicular to the core axis. They are composed of very fine-grained chlorite ± clay rich zones that are separated by fractured light-colored regions of fractured protolith. **D)** Sample LE 4-130 from the edge of the damage zone of the interpreted primary fault zone. The rock is primarily damaged rock with web-like fractures throughout, with narrow slip surfaces near the top that are at high angles to the core a. Primary quartz-feldspar-rich protolith lies in the upper two-thirds of the core image.

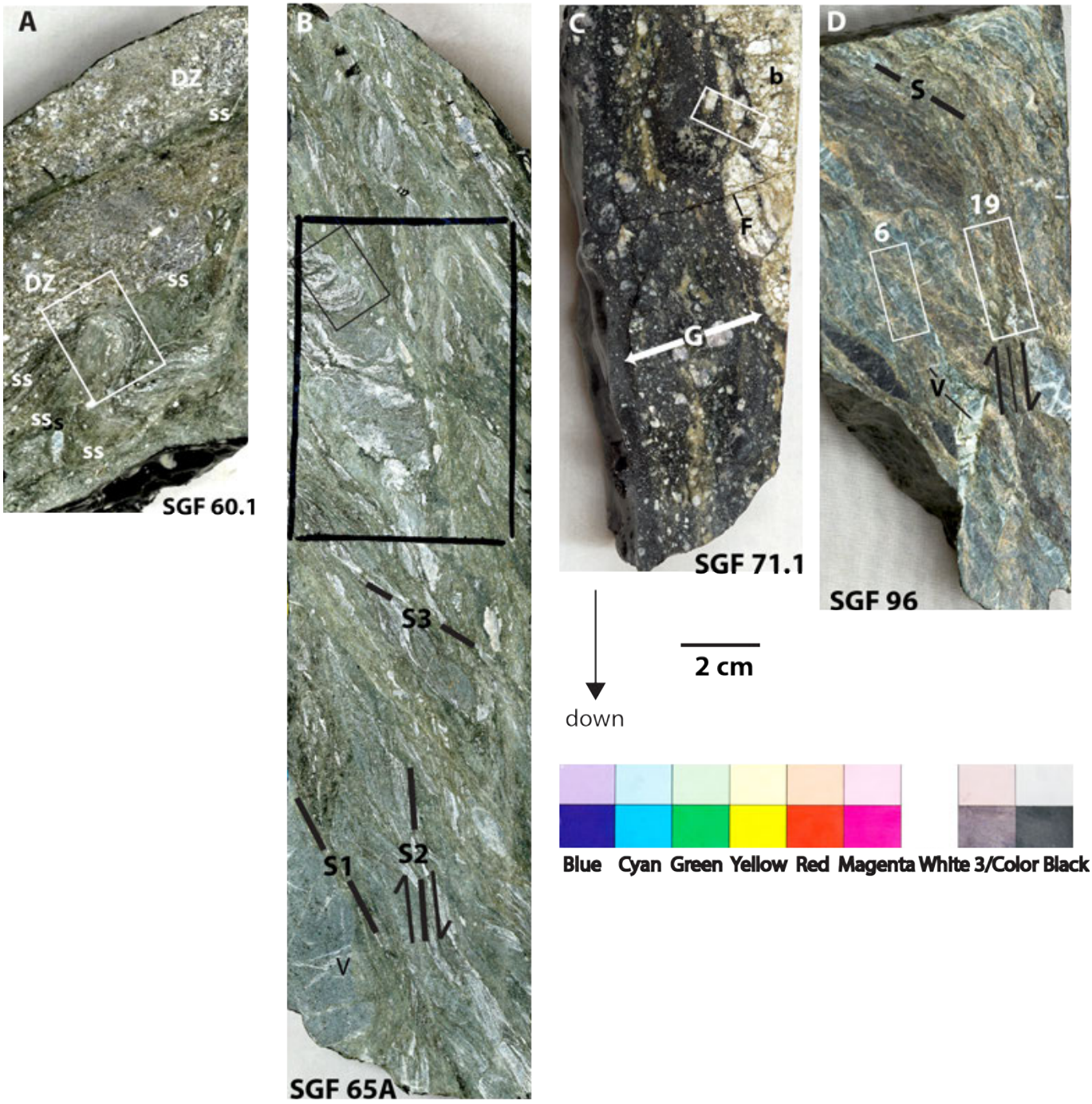

Figure 4 – Images of unoriented ALT B2 core sections across the San Gabriel Fault zone. Deformed zones exhibit finely foliated sheared zones with small angles between the fabrics and the core axis. Figures A, B, and C are from the area next to and within the upper fault zone. **A)** Sample SGF 60.1. Damaged rocks (DZ) consist of zones of light gneissic protolith and dark chlorite-rich alteration. The sample is cut by shallowly dipping, mm-thick slip surfaces (ss) composed of dark green cataclasite. The area in the white box shown in Figures 6 and 14 consists of folded foliated cataclasite and calcite veins juxtaposed against the wall rock damage zone gneiss. **B)** Sample SGF 65A of highly sheared chlorite + carbonate + zeolite in the fault core. A steep foliation S1 is cut by the nearly vertical foliation S2, which exhibits a down on the right of sense of shear is cut by the shallow S3 shear surfaces. The lighter-colored regions are lozenges of calcite ± zeolites. Small isoclinal folds sampled by thin sections and XRF-maps are described below. Note sharp planar veins (v) in the lower part of the core that cut a sheared rock section at a high angle to the foliation. The regions examined with the XRF mapping (small box) consist of a folded, rounded fragment of calcite and chloritic sheared rock cut by the S1 foliation. The large box drawn on the core shows the location of a large thin section from the sample. **C)** Sample 71.1 of light-colored brecciated quartzo-feldspathic wall rocks cut by dark gouge (g) and cataclasites with angular light-colored fragments. The area examined with XRF mapping, indicated by the box, encompasses brittly deformed host rocks, where fractures (F) filled with dark material are at a high angle to the gouge zone. The white wall rock also exhibits a breccia (b) with angular fragments bounded by light-brown filled fractures. **D)** Sample SGF 96 of highly sheared rock with thin slip surfaces from the lower fault zone in the San Gabriel fault near the base of the borehole. Chloritic, foliated cataclasite is mineralized by calcite and zeolite in the foliated rocks (S) cut by a slip surface in the box examined in Figure 19. Sharp, planar calcite veins (V) are in clasts within the foliated zone and cut the foliated zone surrounding the region imaged in Figure 6.

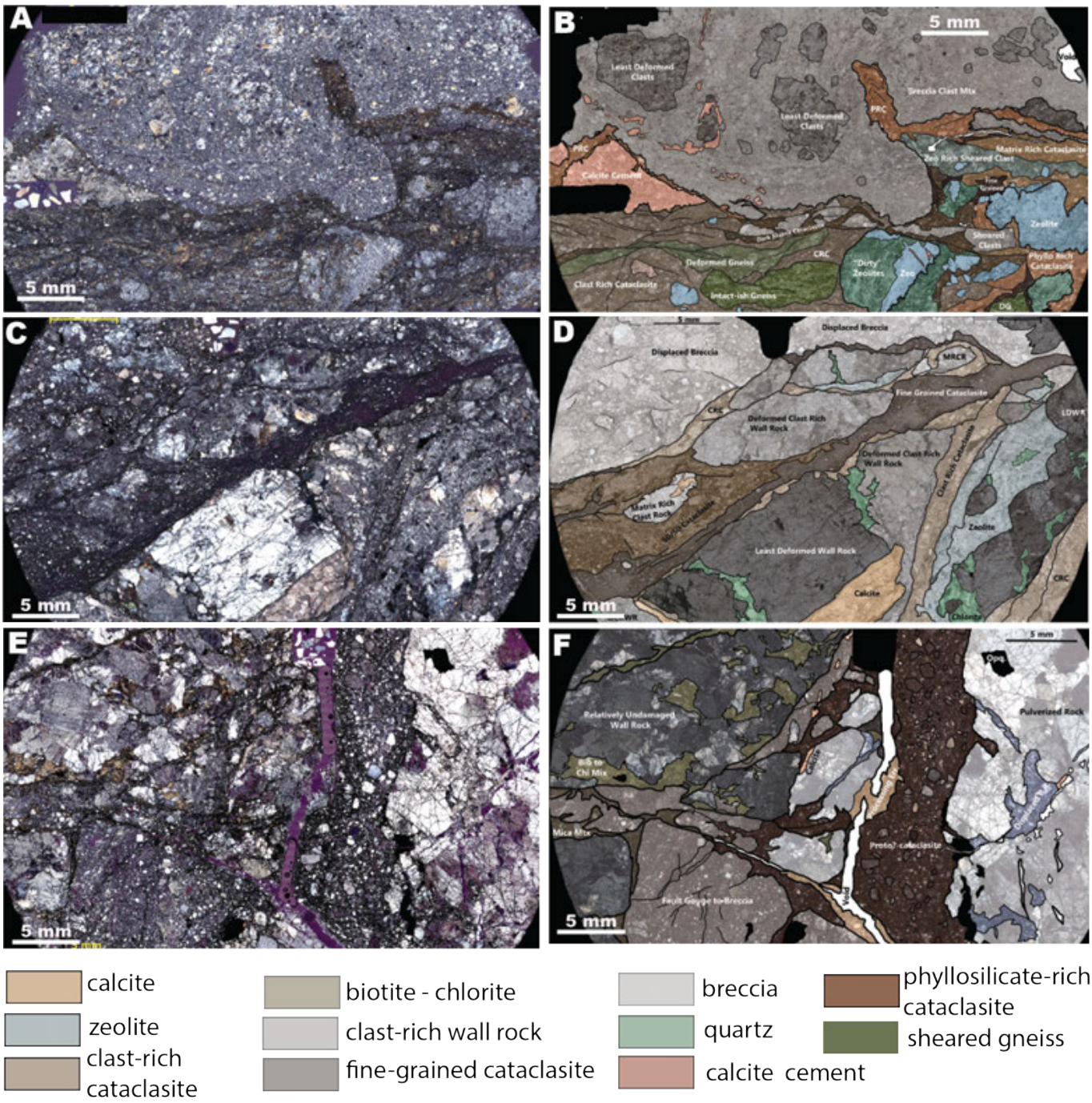

Figure 5 – Microstructures and textures of the deformed and altered rocks in the San Andreas Fault damage zone sampled by the Lake Elizabeth boreholes. **A)** Cross-polarized photomicrograph of sample 3-275. **B)** Annotated map of the image in A. The random fabric fault gouges in the upper part of the image are composed of a breccia clast-rich matrix with more prominent, rounded clasts of less-deformed entrained cataclasite clasts. The breccia is cut by dark brown foliated cataclasite derived from the host gneiss. This foliated rook contains subrounded and irregular fragments of zeolite-rich clasts, calcite, sheared fragments, and phyllosilicate-rick cataclasite (PRC). Some of the phyllosilicate-rich cataclasite was injected into the gouge. **C)** Cross-polarized photomicrograph of sample 5-184. **D)** Annotated map of the image in C. Complex fault-alteration relationships show that several generations of cataclasites and zeolite cut angular-fragment breccias. Small zones of fragment-rich zones lie on the edges of the cataclasite. **E)** Cross-polarized photomicrograph of sample 5-367. **F)** Annotated map of the image in E. Pulverized fault-related rocks (right side of image) is cut by dark, fine-grained cataclasite, which also cuts deformed protolith that shows biotite altered to chlorite. Thin, planar fractures filled with cataclasite have sharp boundaries that cut the deformed host rock and fragments of breccia and gouge.

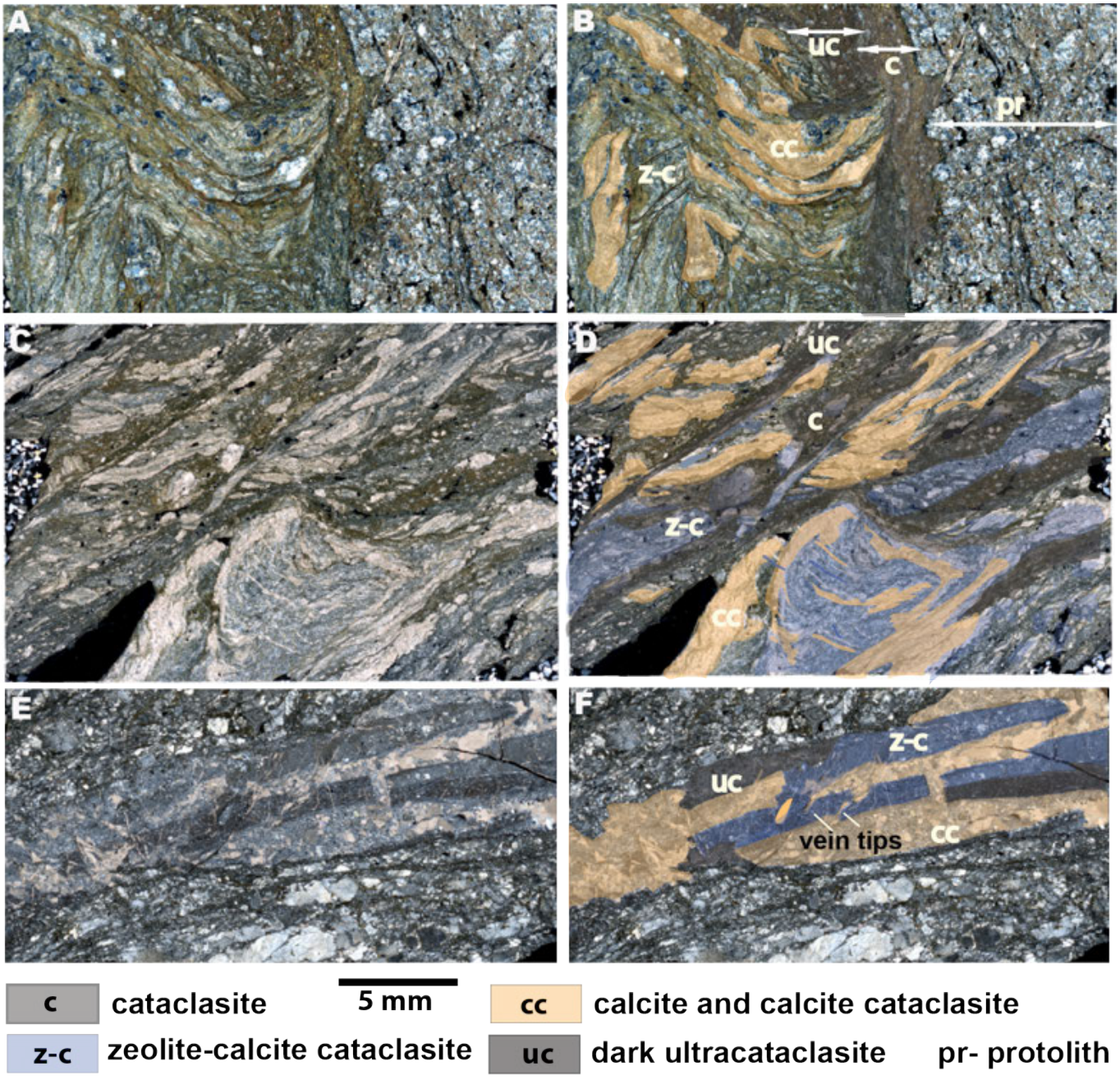

Figure 6 – Examples of microstructures and textures from the sheared and altered damage zones of the San Gabriel Fault in the ALT-B2 borehole. **A)** Cross-polarized photomicrograph of sample 60.1, in the upper damage zone. **B)** Annotated map of the image in A. The sample exhibits a deformed protolith (pr) with a weak foliation marked by aligned, brown altered biotite grains. Cataclasite (c) and ultracataclasite (uc) cut the protolith and folded sequence of calcite and zeolite- calcite ± chlorite. Thin, dark slip zones shear folded folio. **C)** Cross-polarized photomicrograph of sample SGF 65.1 in the upper damage zone. Foliated cataclasite is comprised of cataclasite and ultracataclasite, with elongate fragments of calcite and calcite+zeolite. **D)** Annotated map of the image in C. Elongate, irregular calcite (cc) lozenges with long axes are parallel to the sheared zones. Thin cataclastic zones are either comprised of dark, iron-rich materials or calcite ± zeolite cataclasite. The rounded fragment at the bottom of the image consists of calcite and zeolite in a rootless fold. Planar calcite veins cut the core of the fragment. These textures indicate that calcite-zeolite mineralization occurred before the development of the cataclasite, likely in layers that were subsequently sheared or as irregular zones. The creation of larger fragments resulted in a 'rollup' structure cut by calcite veins that do not exhibit evidence of folding. **E)** Cross-polarized photomicrograph of sample SGF 96, from the lower damage zone. **F)** Annotated map of the image in E. Planar foliation is defined by ultracataclasite (uc) cut by calcite fragment rich, random fabric cataclasite (cc) and zeolite-calcite (z-c) cataclasite. The sharp boundaries, right-angled structure, vein tips, and random fabric nature of the calcite-rich cataclasite suggest that it may have fluidized or been at high pressures when it cut the earlier formed cataclasite. Details of the microstructures are provided in *Crouch and Evans* (2023).

the textures and distribution of calcite ± zeolite (Figures 6A-D). Folded, Interlayered carbonate and zeolite layers are cut by Fe-rich cataclasite (Figure 6A, B). Near the fault zone, the sheared rocks are comprised of mm-thick shear zones that cut lozenges of calcite entrained in cataclasites with fragments of quartz, zeolite, and calcite (Figures 6C, D). Large, rounded clasts of calcite and zeolite within the sheared rocks (Figure 6D) and planar calcite veins within these rounded clasts indicate that alteration was followed by rounding, the development of veins, and transport of the clasts (Figure 6D).

Microstructures from the San Gabriel Fault exhibit planar fabrics with sharp corners and fracture tips (Figure 6F). Sheared and altered granitic rocks show fractures and low-temperature plastic deformation in the form of undulose extinction (Figure 6C). Sub-mm thick cataclasite zones cut these semi-brittly deformed rocks, along with zones of cataclasite dominated by angular calcite fragments and fine-grained zones composed of zeolite fragments. These zones cut Other fine-grained cataclasites at right angles to the foliation (Figure 6D). The calcite-rich cataclasites exhibit narrow, angular tips that cut into the cataclasites (Figure 6D).

5.2 Geochemical Analyses of Fault-Related Rocks

The whole-rock geochemical analyses of major-, minor-, and trace-element data for the rocks in the two fault zones of rocks help constrain, at the cm- to mm-scales, the nature of chemical changes associated with deformation in and around the fault zones (see data tables here: Table 1 and Table 2). The samples were initially grouped into textural categories based on mesoscopic and microscopic textures and mineralogy (*Crouch and Evans*, 2023; *Studnicky*, 2021). These categories (Figure 7) were then refined and used to further our evaluation of the nature of alteration in the faults (Figures 8 and 9).

The whole-rock geochemistry data defines two initial end-member rock types in the San Andreas Fault zone (Figure 7A). The amphibolite gneiss protolith described in the field (*Hernandez*, 2011; *Williams et al.*, 2021) is distinguished by high Fe, Ca, Mg, Ti, P, and loss on ignition values (Figure 7A). The core descriptions, optical petrography, and mineralogical analyses (*Studnicky*, 2021) show that this is a hornblende-biotite-plagioclase gneiss, likely derived from the southwest side of the fault zone. At the other end of the spectrum are rocks enriched to ~80 wt% Si and with meager amounts of all other major elements. These rocks are drawn from a light-colored pulverized rock that exhibits a random fabric texture (*Ostermeijer et al.*, 2022; *Dor et al.*, 2006; *Studnicky*, 2021) and low-temperature alteration of alkali feldspars and hematite alteration (*Aben et al.*, in press). Three other rock types based on their mesoscopic and microscopic textures and mineralogy (*Studnicky*, 2021; *Williams et al.*, 2021; *LADWP*, 2019) are defined: a quartzo-feldspathic (QF) protolith, fault-damage zone rocks, and highly seared cataclasite and gouge (Figure 7a). These are geochemically similar - the QF protolith is slightly depleted in Fe and enriched in Na relative to fault gouge and cataclasites, which are somewhat enriched in iron and depleted in calcium.

The core across the San Gabriel Fault zone reveals six rock types based on core and microscopic-scale textural and compositional characteristics (*Crouch and Evans*, 2023). The amphibolite gneiss protolith (Figure 7B) is enriched in iron, titanium, and phosphorous; the granodiorite protolith is low in iron, calcium, magnesium, and phosphorous. These rocks are likely derived from the Mendenhall Gneiss (separated into amphibolite and quartzo-feldspathic protoliths) and Josephine Granodiorite protolith. Two compositional types of damage zones are documented in the core (*Crouch and Evans*, 2023): a gneissic damage zone rocks north of the SGF from 120-313 mmd in the borehole, and a granodiorite damage zone south of the SGF from 325-465.5 mmd. Damage zone rocks have higher Fe, Ca, and loss values on ignition components (LOI; typically the result of the presence of CO^2, H^2O, OH in clays, and of organic matter) than the protoliths (Figure 7b). The damage zone rocks exhibit a range of values of loss on ignition (LOI) constituents from <1 to 8 wt%.

The fault gouge rocks have relatively high Fe, Ca, and LOI values relative to the quartzofeldspathic protoliths but are commonly less than the damage zone samples' values (Figure 7). The damage zone and highly sheared rocks from the principal slip surfaces are depleted in Si (Figure 7B) relative to the protoliths.

Cross plots of major cations Fe, Ca, Mg, and LOI values as a function of SiO_2 amongst the different rock types (Figures 8 and 9) help determine the nature of fluid-rock interactions (see *Williams et al.*, 2021). Elements Al, K, and Na do not exhibit any trends in relationship to the Si values (*Studnicky*, 2021), so we focus on the Fe, Ca, Mg, and LOI values here. The pulverized rocks in the San Andreas samples are uniquely defined by very low Fe, Ca, Mg, and LOI values (Figure 8). In contrast, the amphibolite gneiss protolith has high values of these components. The quartzofeldspathic protolith exhibits intermediate values in the cations and very low LOI values. Damage zone samples exhibit a significant dispersion of Fe and Ca, with several samples > 8 wt% (Figure 8A, B). The Mg values in the damage zone rocks are not significantly different from the protoliths, and the LOI values are between 2 and 8 wt%, greater than the quartzofeldspathic protoliths. Damage zone rocks exhibit slightly lower values of Fe and Ca relative to the amphibolite protolith. The LOI values of the damage zone and gouge samples are higher than those of the QF-protolith and increase with decreasing SiO_2. Samples of fault gouge here also exhibit intermediate

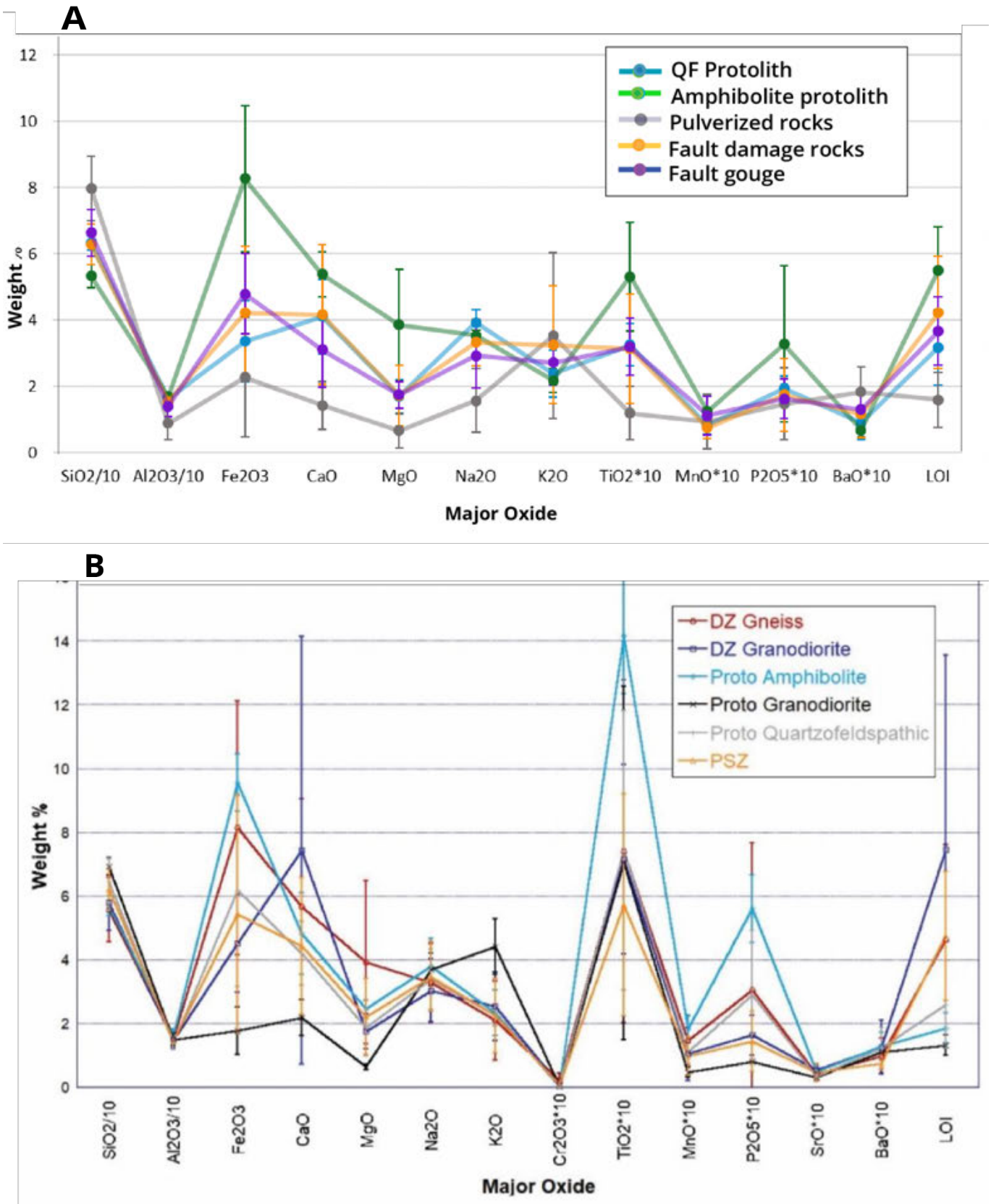

Figure 7 – Whole-rock major element geochemical data for the San Andreas and San Gabriel fault zones with two standard errors. The rock type categories are based on mesoscopic and microtomic studies of the rocks (*Crouch and Evans*, 2023; *Studnicky*, 2021). **A)** The Lake Elizabeth site results. The end-member amphibolite gneiss and the pulverized rocks are defined by high values of Fe, Mg, Ca, and Mn for the gneiss and extremely high Si values and low Fe, Mg, and Mn values for the pulverized rocks. The quartzo-feldspathic protolith (QF), Fault damage zone rocks (DZ), and fault gouge cluster together and exhibit intermediate values of major elements. **B)** Whole rock geochemical data for the San Gabriel Fault. The amphibolite gneiss is distinguished by high Fe, Ti, and P values, whereas the granodiorite protolith is low in Fe and Ca. The LOI values are 2-5% higher in damaged and altered rock than in protolith. The granodiorite damage zone shows 5% higher Ca values than the protolith, and the gneissic damage zone shows <2% higher Ca values.

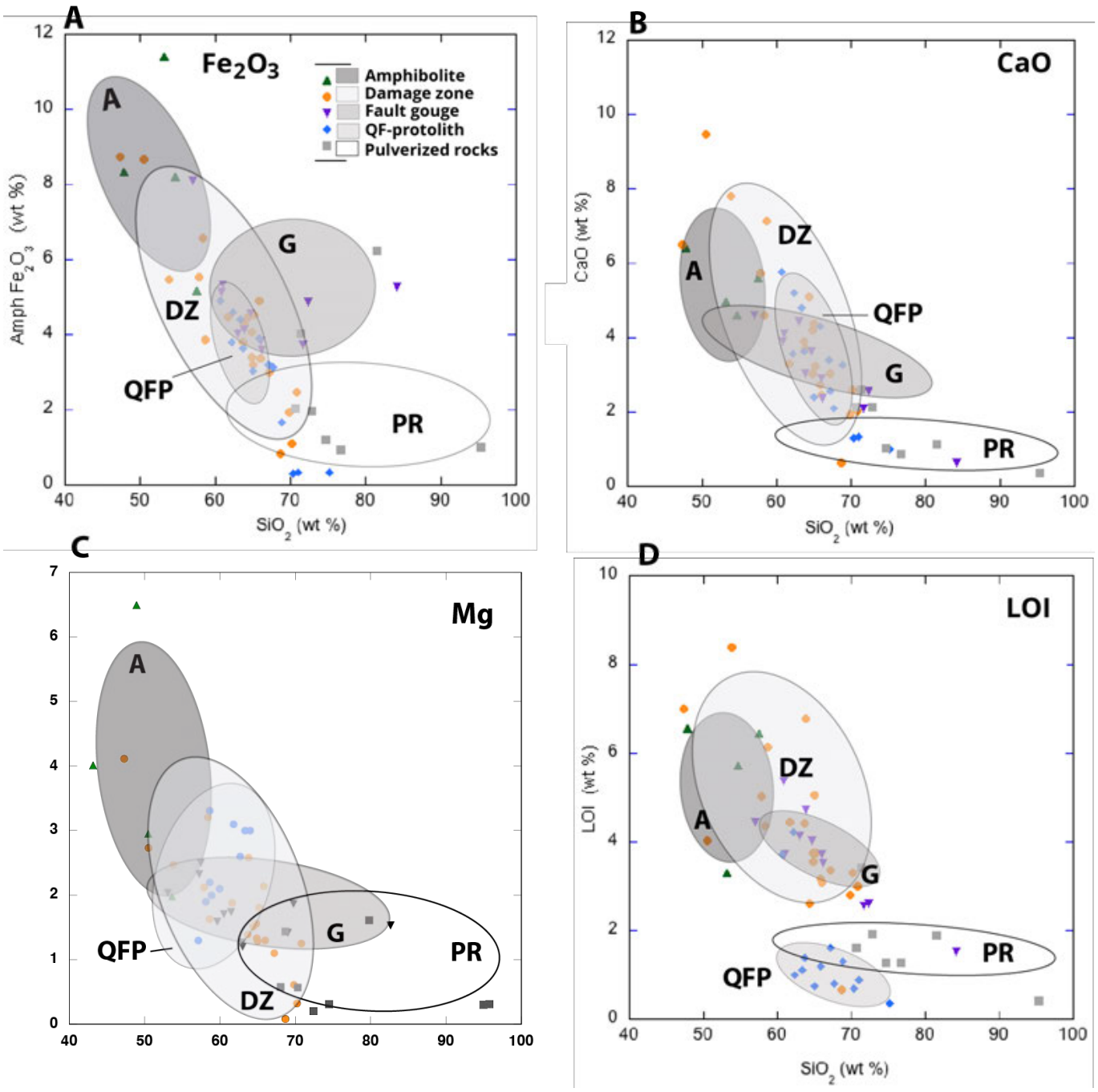

Figure 8 – Cross plots of the whole-rock geochemical analyses for Fe, Ca, Na, and loss-on-ignition values and the results of bootstrap analysis for the Lake Elizabeth site. The ellipses are the 90% confidence uncertainty ellipses that identify likely elemental groups based on the bootstrap analyses for samples from the San Andreas Fault. Due to differences in the axes' scales, the covariance ellipses are distorted, but the major and minor axes are scaled appropriately. Major oxides are plotted against SiO_2. The rock types determined from the microscopic nature of textures and mineralogy and X-ray diffraction analyses are also differentiated by the whole-rock chemistry. **A)** Total Fe, reported as Fe_2O_3, as a function of SiO_2. **B)** CaO as a function of SiO_2. **C)** Na as a function of SiO_2. **D)** Loss on ignition as a function of SiO_2. The error ellipses show that the fault damage rocks (DZ) and gouge exhibit Fe, Na, and LOI values that are intermediate between the amphibolite and quartzo-feldspathic protoliths. The Ca in the damage zones rocks is enriched relative to the other rock types.

values of the cations, with less dispersion than the damage zone samples and a mean value of LOI of slightly less than four wt%. Damage zone, gault gouge, and QF protoliths exhibit similar Mg values, and the damage zone and fault-related rocks have LOI values of 4-6 wt%.

Samples from the San Gabriel Fault display relatively clear definitions of the amphibolite and the quartz-feldspathic protoliths (Figure 9). We combine two QF-protoliths defined by *Crouch and Evans* (2023) into one group due to the similar values and few analyses for each group. The amphibolite is high in iron (Figure 9A), has moderate amounts of Ca and Mg, and has low values of loss on ignition components (Figure 9B-D). The quartzofeldspathic protolith also has low values of LOI, along with low values of Fe, Mg, and Ca. Damage zone and gouge samples exhibit a

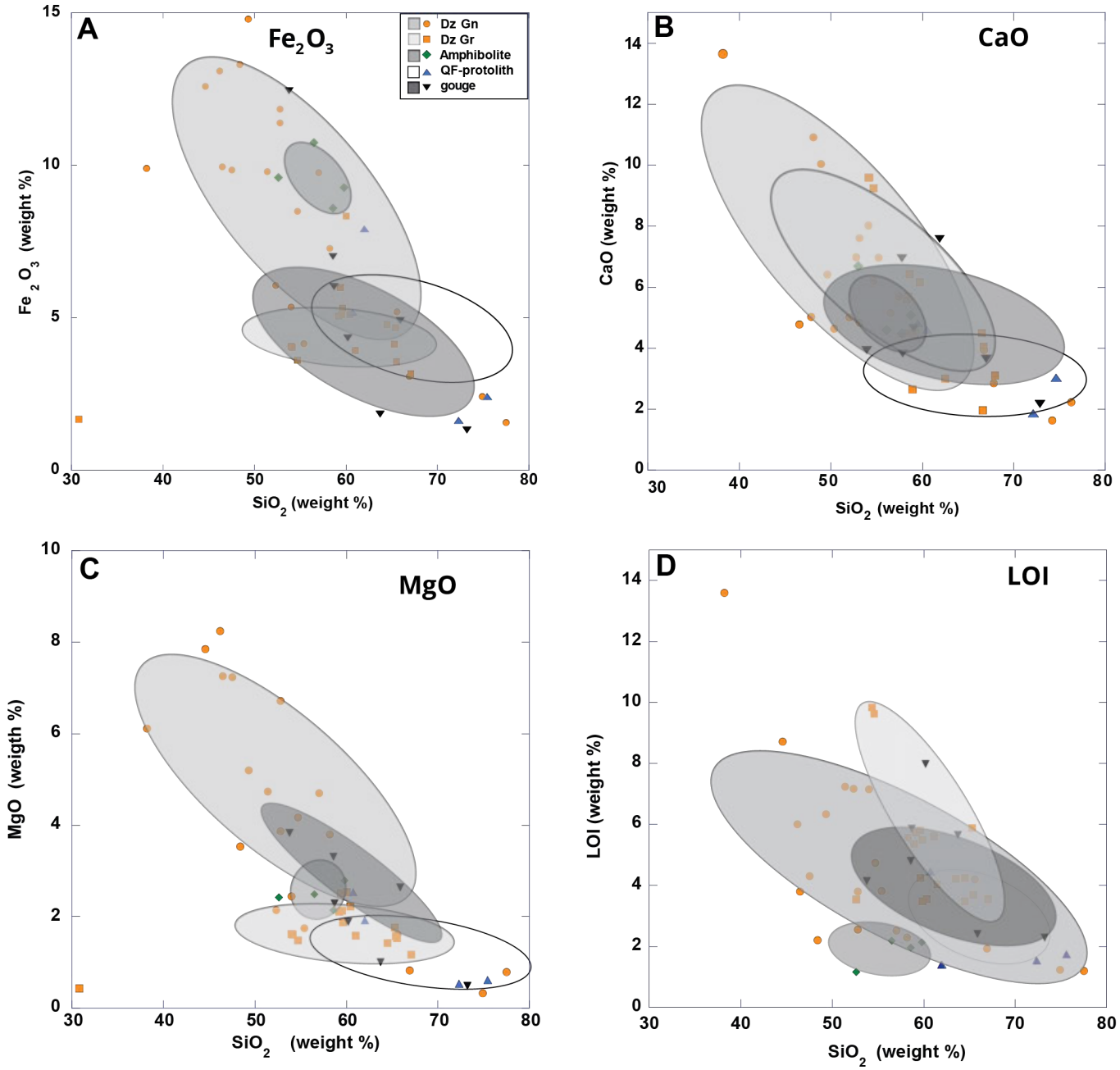

Figure 9 – Scatter plots of the whole-rock geochemical analyses for Fe, Ca, Mg, and loss-on-ignition (LOI) values and the results of covariance analysis for the San Gabriel fault site. The ellipses are the 90% confidence uncertainty ellipses that define likely element groups of the samples. Principal oxides are plotted against SiO_2. The rock types determined from the microscopic nature of textures and mineralogy and X-ray diffraction analyses are differentiated by the whole-rock chemistry. **A)** Total Fe, reported as Fe_2O_3, as a function of SiO_2. **B)** CaO as a function of SiO_2. **C)** Mg as a function of SiO_2. **D)** Loss on ignition as a function of SiO_2. The error ellipses show that the fault gouge values are enriched in Fe, Ca, Mg, and LOI relative to protolith and damage zone rocks. Damage zone rock values of Fe and LOI values are intermediate between the protolith values.

wide range of major element values. The damage zones have Fe values as high as 15 wt% (Figure 9A) and a minimum of ~2 wt%. Calcium is as high as ~14 wt%, and the gneissic damage zone samples exhibit a stronger inverse relationship between Ca, Fe, and Mg. LOI and Si then do the granodiorite damage zone samples (Figure 9). Gouge samples exhibit a smaller range and low cation values (Figures 9A-C) and a slight enrichment in LOI values (Figure 9D). The whole-rock data indicate that cataclasite and gouge samples reflect a mixing of the protoliths and damage zone samples.

The trace- and rare-earth element data track variations in the geochemistry of the fault-related (Figure 10; Figure SI-1, Supporting Information) enable us to directly compare values from different fault-related rocks across the fault zones by comparing the data for individual samples relative to reference protolith value. The mean values of protoliths from 16 samples of quartzo-feldspathic gneiss and amphibolite gneiss (see data table here: Table 3) provide a reference value. Thus, we

normalize our data to this local standard (*Rollinson et al.*, 2021):

$$Enrichment\,factor = \frac{deformed\,rock\,value}{protolith\,value} \quad (1)$$

The rocks from the damage zone of the San Andreas Fault are enriched in V, Cs, Th, and Th relative to the local protolith; the fault gouge rocks are exhibit higher values of enrichment (Figure 10A). The elements from Zr to Pr exhibit slight enrichments that are a maximum at Cs. The San Gabriel Fault zone rocks are enriched in Cr, Cs, Th, and U, and samples from the principal slip zones are high in V, Cs, , and Th, relative to the nearby protoliths (Figure 10B). The trace element distribution patterns (Figure 10) can be sorted into three broad categories: 1) lithophile elements Cs and associated elements 2) transition elements V and Cr; and 3) thorium and, to a lesser degree, uranium enrichment.

5.3 X-ray Fluorescence Maps

The deformation textures and nature of alteration assemblages in these rocks (*Crouch and Evans*, 2023; *Studnicky*, 2021) indicate that moderate to significant alteration and mineralization occurred during fault development at the drill core, thin-section, and 2-g sample scales. However, it is difficult to determine the detailed spatial relationships between the alteration assemblages and the deformation textures without high-resolution images of the deformed rocks that relate deformation textures with compositional variations. The XRF-based elemental mapping helps to determine the grain-scale nature of this alteration and its relationship to deformation textures. Samples for XRF mapping were selected based on their optical deformation and mineralization character and for the evidence of moderate to significant amounts of Fe, Ca, Mg, and, in some cases, Mn content based on the whole rock and petrographic studies.

5.3.1 Damage Zone Rocks

We first examine a ~60 cm long section of drill core from a portion of the SAF damage zone (Figure 11) with XRF-macroscale mapping to determine the core-scale relationships between alteration, mineralization, and deformation in the damage zone. The sample comprises several narrow, dark zones comprising foliated cataclasites, fine-grained indurated fault gouge, distributed green-gray alteration products (Figure 11A) in feldspar-rich fractured and sheared damage zone rocks, and several zones of less altered protolith.

The chalky white and green protolith appears to consist of altered K- and Na-feldspar – hornblende gneiss cut by green-dark grey-red fault zones 1-5 cm thick, surrounded by white to red fractured rocks (Figure 11A) and indurated narrow red and green zones of concentrated slip. The distribution of iron throughout the damage zone matrix (Figure 11b) denotes iron-rich, coated, filled fractures and mm- to cm-thick, Fe-rich cataclastic zones. The fracture networks exhibit relatively straight fractures, whereas the bulk of the damage zone imaged reveals irregular Fe-rich zones. Iron-rich damage zones are characterized by 1-3 cm thick zones with mm- to cm-scale protolith clast distributed within them (Figure 11C). Cataclasite zones are 5–10 cm wide and have up to 8 wt% Fe and Ca are concentrated along planar fractures and in through-going zones with distrusted iron (Figure 11B1). The distribution of transition elements Cr, Mn, Ca, and K (Figure 11C, D; Figure SI-1, Supporting Information) reflect elemental variations that may mark fluid pathways. Manganese closely correlates with Fe (Figure SI-1, Supporting Information), and V lies in irregular zones (Figure 11C) typically associated with K (Figure 4D) and with Ti in small, elongated regions. Downhole, Ti is common as small equant zones, perhaps reflecting the presence of titanite. Irregular K-rich areas are associated with chalky white zones, and Cr is distributed through the sample in small irregular zones (Figure 11D). Small Ca-rich veins (Figure 11D) cutting the host rock consist of fractured potassic feldspar zones.

The textures and element distribution in the damage zone rocks (Figures 12-14) reveal micron-scale elemental concentrations and distinct variations in these concentrations over the micro-scale in both fault zones. Rocks from the damage zones that likely reflect early or lesser stages of deformation (Figures 12 and 13) contain mm-thick transgranular fractures and slip surfaces (Figure 12a) that weave through the fractured protolith feldspar grains (Figures 12b-e and 13). In places, fractures are at high angles to these surfaces (Figure 12), filled with cataclasite or trace amounts of metals. Thin fractures emanate from some slip surfaces with sharp tips. The slip zones contain rounded deformed protolith and cataclasite clasts in a fine-grained matrix enriched in Fe, Mn, Ti, and Cr. Planar intragranular fractures in plagioclase grains are enriched in these elements and, in some places, significantly enriched (see, for example, the Ti, Mn, and Cr maps in Figure 12b). These metal element-filled cross fractures define smaller angular grains that represent angular fragments. The trace elements Ti, Mn, and Cr lie in narrow surfaces and mm-scale pods (Figures 12 and 13). The damage zone sample from the San Gabriel Fault appears relatively undeformed at the drill core scale. Yet, in the XRF maps, the distribution of Cr, Mn, and Ni indicates the presence of fractures in the feldspar-rich sections (Figure 12d), and these relationships continue in more deformed rocks.

The transition from protolith to faulted rocks consist of fracture networks adjacent to and within small-displacement faults (Figure 12) with significant iron concentrations that define the networks (Figure 12B). Calcium is distributed in the fracture networks (Figure 12D), and Fe permeates the rocks at the

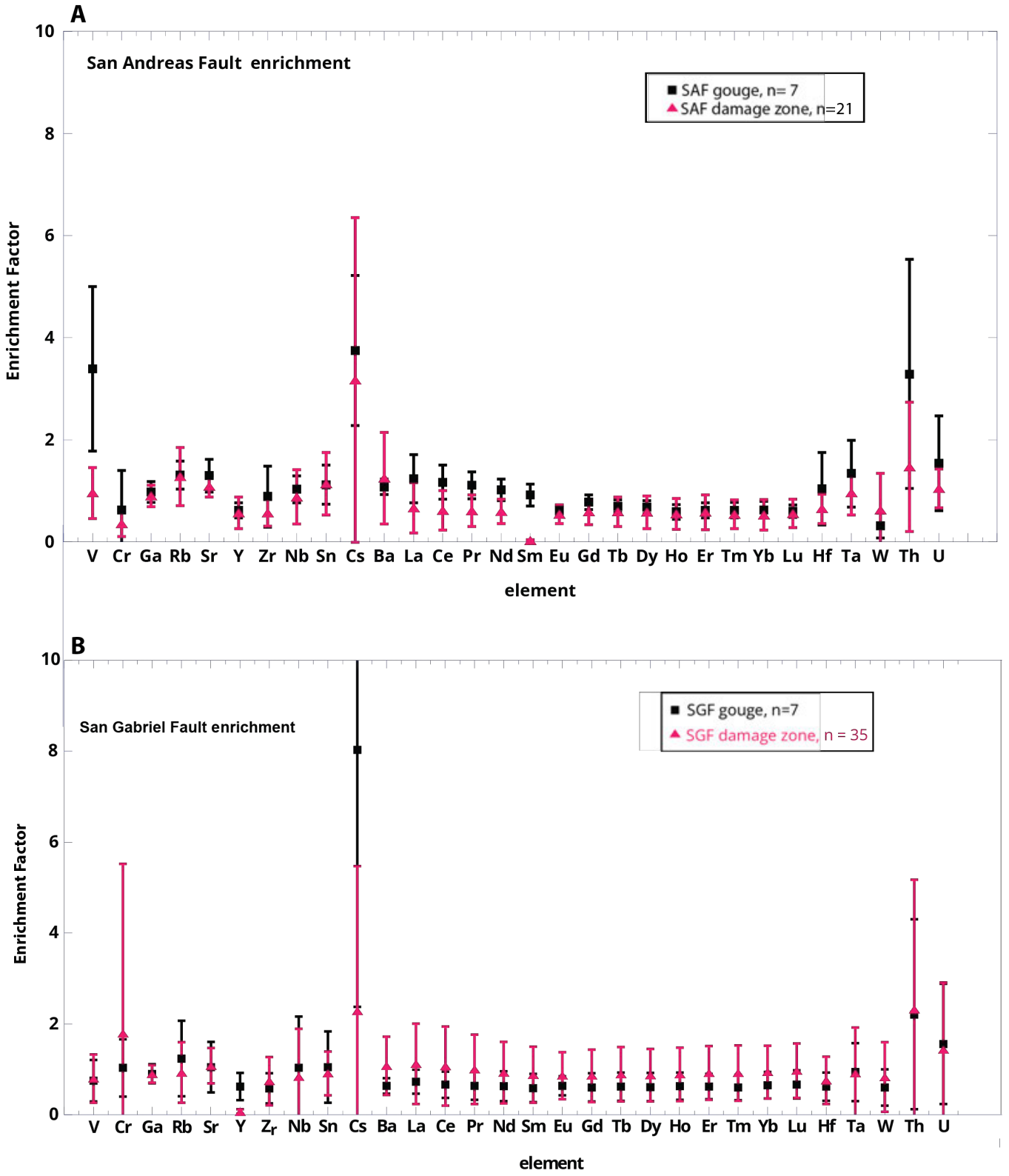

Figure 10 – Rare earth and trace element enrichment data for samples from the damage zone and fault zone rocks of the San Andreas and San Gabriel Faults. **A)** Averages of the enrichment factors for fault core and damaged zone rocks from the San Andreas Fault. Slight enrichments in the damage zone occur in V and Th, and the fault gouge is enriched in V, Cs, and Th, with depletions in Y, Eu, and W. **B)** Averages of the enrichment factors for damaged zone and fault core rocks from the San Gabriel Fault. Significant enrichments in Cr, Cs, and Th, and modest enrichment in U are observed.

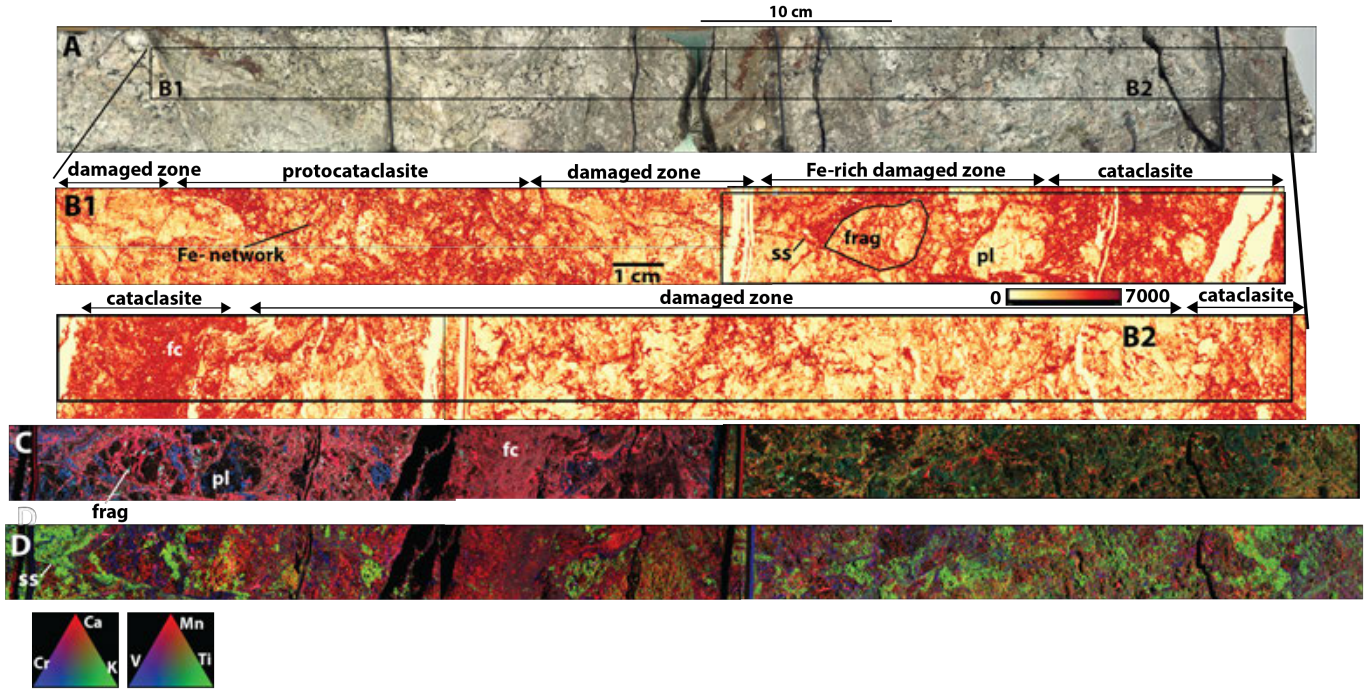

Figure 11 – Macroscopic X-ray fluorescence maps of a portion of the core sample 3-189 (core depth of 58 m; vertical depth 36 m) extracted from directly beneath the intensely damaged zone below and north of the main fault zone of the San Andreas Fault. The protolith consists of granodiorite gneiss. Thin, vertical black ones are mounting wires or gaps in the core. **A)** Optical image of the entire core section with the zone examined in the X-ray map outlined in the rectangular box. The 60-cm long and 5-cm diameter sample was examined at beamline 6-2 at SSRL (see *Edwards et al.*, 2018). The chalky white regions are feldspars, most exhibiting core-scale alteration textures, green-gray cataclasite zones, and deep red regions of iron alteration and mineralization. **B)** Map of iron in the analyzed section. The scale is counts/second. The rectangles indicate the areas mapped in Figures C and D. B1 – light-colored regions are relatively low in Fe contents, associated with the light-colored zones of gneissic protolith seen in A. Feldspar-rich fragments (frag) are cut by intergranular Fe-filled fractures, and relatively intact plagioclase grains (pl) of iron enrichment include fracture networks with high iron content along the fractures and zones with high iron content along the fractures, and zones highly enriched cataclastic zones (cata) that consist of fine-grained, amorphous Fe-rich zones. B2 – Foliated cataclasites (fc) are iron rich, and damage zone rocks consist of irregular zones likely comprised of damaged feldspar and altered hornblende + biotite grains **C)** Tricolor map of Ca, Cr, and K distribution in the rocks, Calcium and Cr are associated with the regions with Fe-fractured filled networks and cataclasite zones; damaged zones region to the right has concentrations of potassium in mottled regions and **D)** Tricolor maps of Mn, Ti, and V distribution in the core. The uphole portion of the core (left) is rich in Mn, and Ti is distributed in irregular zones. The downhole portions are less enriched in Mn. The lower region contains irregular zones of V and K, with small regions of Ti concentrations. The foliated cataclasite zone is enriched in Ca and Mn.

sub-mm scale (Figure 12C). The anti-correlation between Ca and Fe is evident (Figure 12D), and Ca appears to be in elongated zones in the fault. The maps show that the fragments in the faults are bound by added Fe, Ca, and other trace elements.

Iron concentrations mark the presence of incipient foliations in fault zones of the San Andreas Fault (Figure 13) along with Ti, Mn, Cr, and Ni (Figures 13B). Slip surfaces several mm to centimeters wide composed of fine-grained cataclasites (Figure 13) form interweaving zones that bound lozenges of protolith in which primary grain boundaries are clearly defined (Figure 13). The protolith lozenges consist of feldspars with varying degrees of alteration, cut by small faults and fractures that are syn- and antithetic to the main mm-thick zones of cataclasite (Figure 13A).

5.3.2 Development of slip surfaces

The evolution of well-developed slip surfaces, cataclastic zones, and faults (Figures 14-19) reveals the significant concentration of the transition elements associated with the development of shear fabrics in the rocks. Early fractures that define weak foliations in the protolith are adjacent to curvilinear zones of cataclasite (Figures 13 and 14). In the upper strand of the San Gabriel Fault, an early, mm-scale foliation defined by thin zones of alteration and cataclasite is folded and truncated by cataclasites (Figure 14B). The cataclasites are enriched in Fe, Mn, Cr, and Ni, and folded and foliated zones contain elongated, irregularly shaped micro breccia fragments with calcite veins (Figure 14).

The evolution from damage zone to sheared faults in the San Andreas Fault is marked by textures of transition element-lined fractures (Figure 15). Micron- to mm-scale fracture networks define block-shaped fragments surrounded by

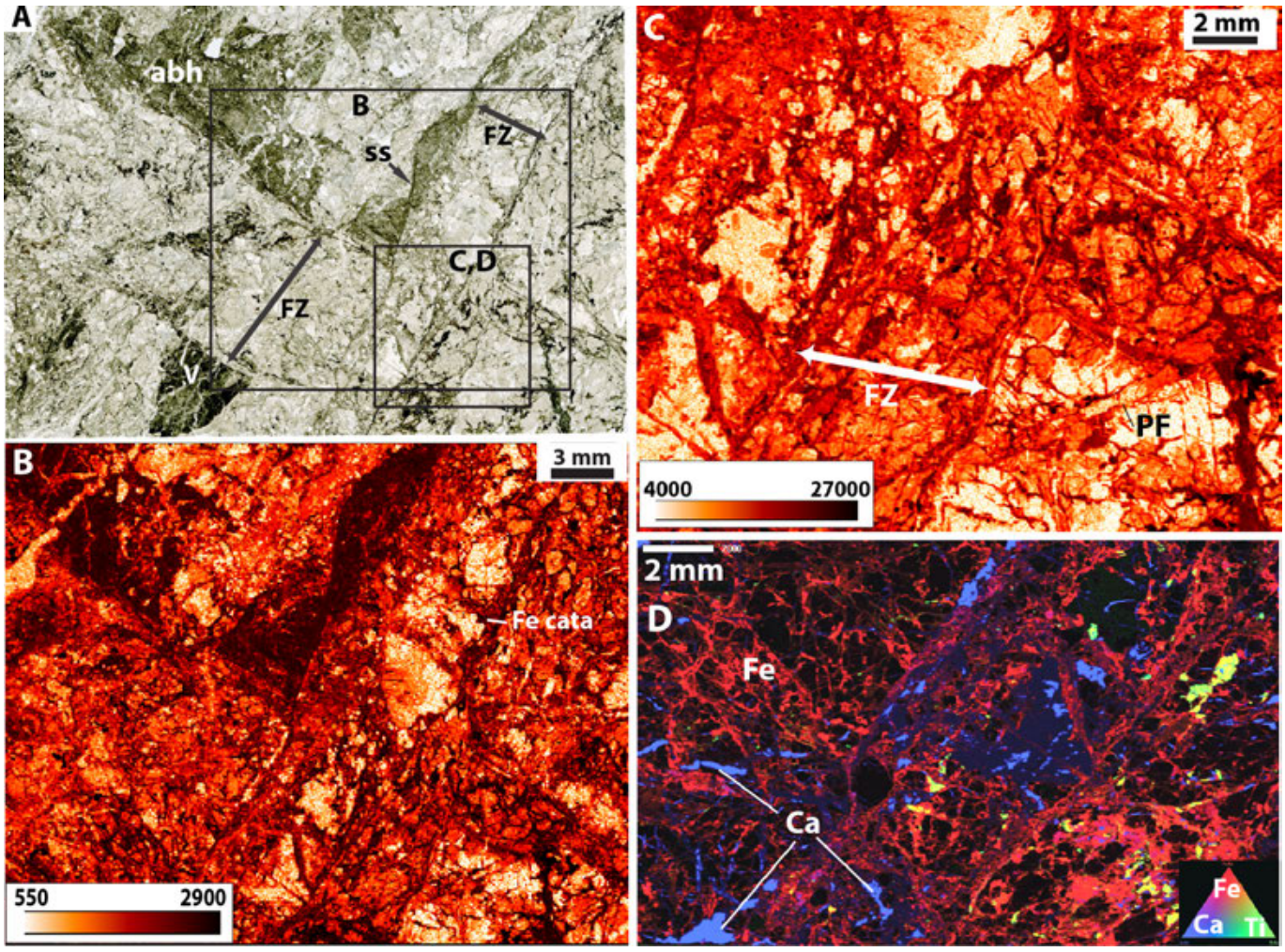

Figure 12 – Microstructures and elemental distribution in sample SGF 71.1 from the upper damage zone of San Gabriel Fault directly adjacent to the likely principle slip zone of the fault (see Figure 4C for the location of these images). Images show the nature of the brittle fracture, faulting, and iron distribution in a damage zone. **A)** Plane-polarized light photomicrograph of the sample (see Figures 2B and 3F for location). The sample contains intact and fractured feldspar (light) and dark hornblende + biotite grains, mostly altered (ABH) and cut by calcite veins (V), small fault zones (Fz) and slip surfaces (ss) that intersect in the middle of the region mapped in Figures B and C. Rectangles indicate the regions examined with XRF mapping. **B)** XRF Iron map of the area shown in A) Iron is concentrated in primary gneiss grains, planar fractures (pf), and fault zones FZ). The Fe is concentrated within fault zones and thin cataclasite zones (fe cata) with angular feldspar fragments in the fault showing the connection between iron-rich regions and the fractures in the fault zone **C)** High-resolution iron map of a region where faults (FZ) intersect and protolith feldspars (light color) are cut by Fe-coated planar fractures. Irregular blebs rich in iron lie within the faults, and iron is disseminated into the feldspar protolith via planar fractures (pf). **D)** A tricolor map of the region in C shows the distribution of iron, calcium, and titanium. The calcium lies in elongate irregular zones at the edges of the cataclasite zones.

the fractures. Iron-oxide and amphibole-biotite grains are sheared and cut by subsidiary fractures (Figure 15), and the Fe, Ti, Cr, and Ni distributions define a 'feeder' texture where the iron-rich zones of the fractured protolith connect to the cataclastic zones. The cataclasite zones are enriched in Ca relative to the host rocks. Correlations amongst the transition metals (Supplemental Figures 2- 4) show Mn increases nonlinearly with Fe, and the Cr, Ni, and Ti increase with Mn in the sheared rocks.

The nature of highly sheared rocks, zeolite, and carbonate mineralization impacts, and the apparent mobilization of transition elements are evident in samples from the San Gabriel Fault, where the fault exhibits a well-developed foliated shear zone (Figure 16). The sheared rocks comprise fine-grained clays, plagioclase, calcite, and zeolites (*Crouch and Evans*, 2023). Rounded lozenges of Ca-rich clasts are embedded in an iron-rich foliated zone and appear to be a rootless Type 2 superposed fold (Figure 16a). Elongate high birefringence lozenges enriched in calcium lie within iron-rich cataclasites (Figure 16b). The pattern of mineralization indicates that earlier calcite veins ± zeolite zones were incorporated into the shear zone, and the transition element distribution appears to be relatively homogenized in the sample, as seen by the frequency of pixels with similar Fe and Mn concentrations (Figure SI-5, Supporting Information).

Both faults exhibit very thin surfaces that suggest

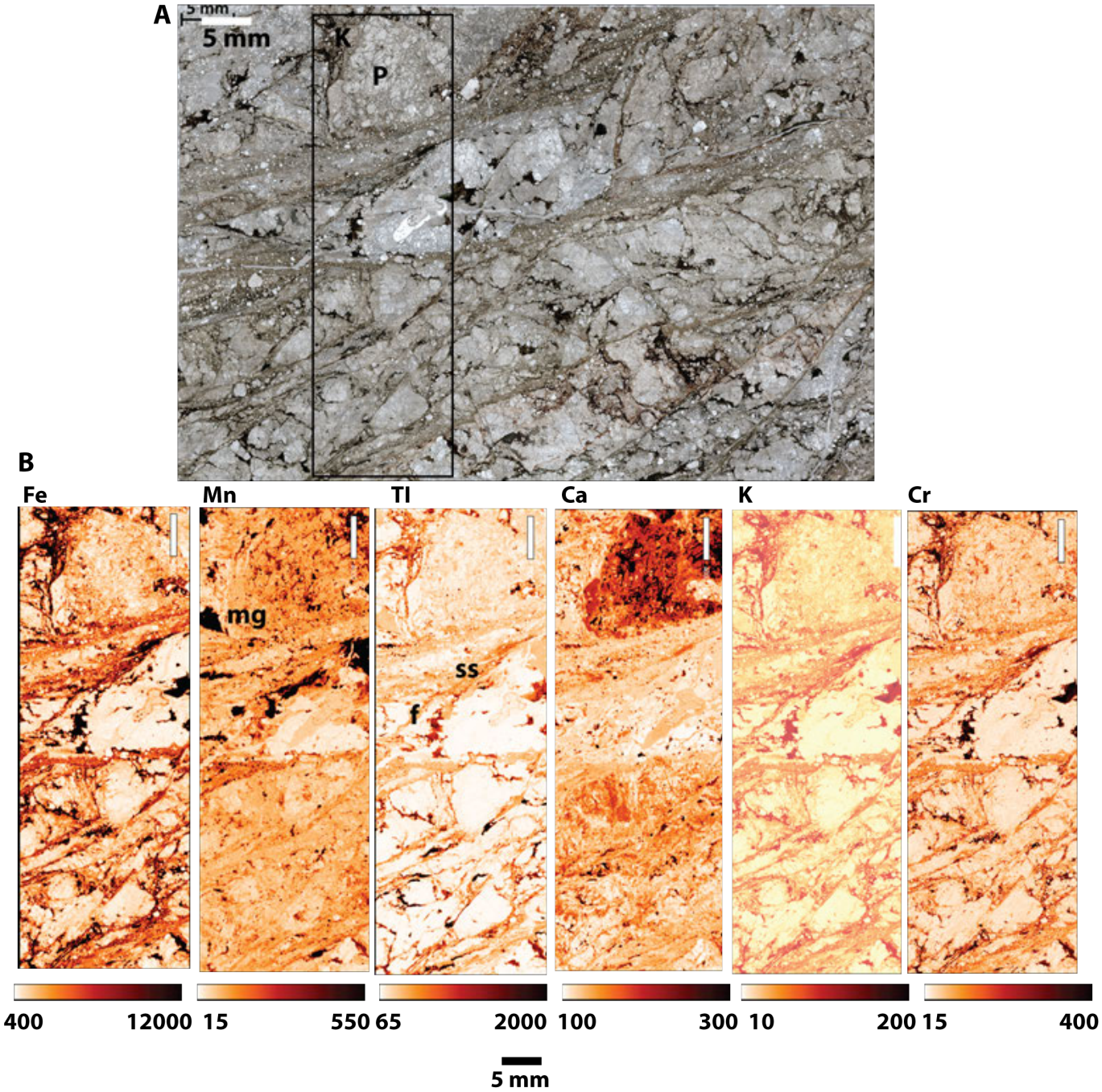

Figure 13 – Microstructures and elemental distribution in sample LE 2-355 of the San Andreas Fault damage zone. See Figures 2A and 3A for the location of this sample. The rock consists of a set of thin slip surfaces (ss) that cut altered and deformed feldspar-rich protolith. **A)** Plane-polarized light photomicrograph of the sample. The rectangle indicates the region examined with XRF mapping. The plagioclase feldspar (P) grains are altered and fractured, and narrow zones of cataclasite (ca) and very thin slip surfaces (ss) dip to the left. Small slip surfaces (red arrows) connect these slip surfaces. Black arrows indicate the small faults antithetic to the slip surfaces, including a zone of cacataclasite injectite (I) with tensile fractures (tf) branching from the cataclasite. **B)** Elemental maps for Fe, Mn, Ti, Ca, and Cr across the part of the sample in the rectangle in A. Iron is distributed in the sheared rock with Ti and appears to originate from equant magnetite grains (mg) with small amounts of Ti, Mn, and Cr, as well as the alteration of mafic grains. Slip surfaces (SS) cut the sample and comprise clay-rich cataclasite. Cataclasite zones are highly enriched in Fe, Mn, Ti, and lesser Cr; thin bands enriched in these elements follow fractures between shear zones. Iron is distributed through the sheared and fractured rocks, and the Ti, Mn, and Cr distribution along fractures, either as nearly continuous linings in the TI and maps or as tiny, concentrated blebs (Cr), defines the intragranular fractures, sheared zones, and intragranular fractures in feldspars. Zones of high Fe-Ti-Mn-Cr concentration are connected to sheared rocks via 'feeder' fracture f. Metal concentrations define fine-scale fracture networks in feldspars.

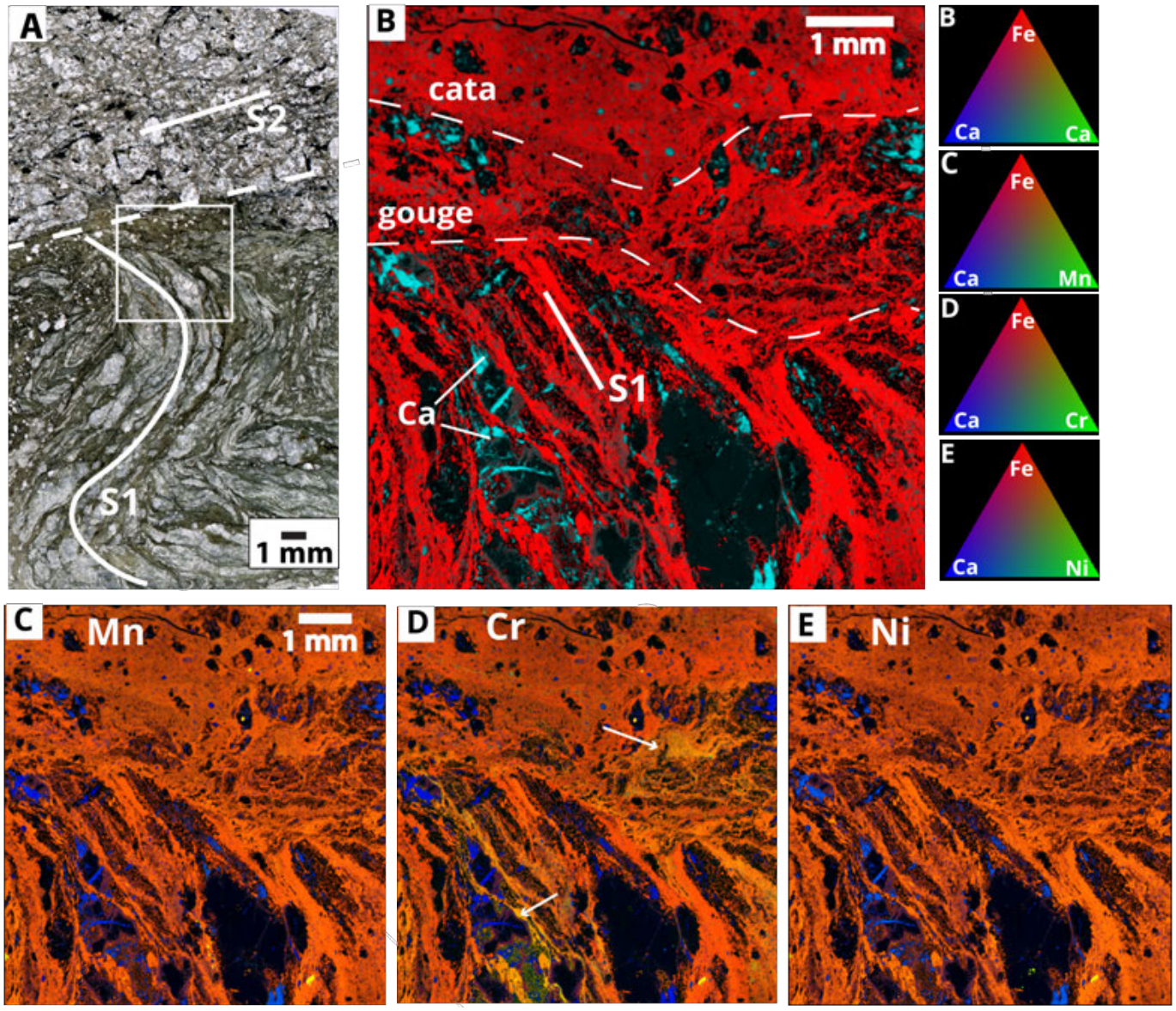

Figure 14 – Microstructures and elemental distribution in sample SGF 60.1 from the ALT-B2 borehole across the San Gabriel Fault. **A)** Plane polarized light image of the thin section that transects damage zone rocks with a weak foliation defined by dark, Fe-lined fractures (F), a dark cataclasite (cata) and folded, foliated carbonate – cataclasite horizons (F2) (See Figure 6 for an annotated image). The cataclasite boundary is marked by the dashed line. The box outline indicates the location of the XRF scans shown in Figures B-E. The triangular scale for B-E shows the color scales for the associated maps. The intensity of red for Fe is the same for all maps, so lighter shades of red indicate contributions of other mapped elements. **B)** Iron-calcium map shows the rocks have a high concentration of iron in a fine-grained zone (cata) and a slightly less Fe-enriched random fabric gouge with clasts of irregular clasts, some of which contain short, planar, calcium-bearing zones, likely demarcating calcite veins. In the foliated zone, elongated feldspar clasts (black in these images) are sometimes cut by intragranular fractures. The calcium in the map here is lighter blue than in Figures C-E because Ca is mapped as blue+green in this image. **C)** Tricolor Fe-Ca-Mn elemental map shows that Mn varies closely with Fe. **D)** Fe-Ca-Cr map shows that in some places, Cr is enriched in thin zones or irregularly shaped regions (indicated by the white arrows). **E)** Fe-Ca-Ni map indicates that Ni is dispersed with Fe and Mn.

extreme slip localization with textural evidence for slip that produced amorphous fault materials. A sample from a relatively isolated 'secondary' fault north of the central fault zone in the San Andreas Fault (Figure 17) sample consists of several sub-mm thick slip surfaces (Figure 17A, B) with significant concentrations of Fe, Mn, Ni, and Ti (Figure 17C). The relatively straight main slip surfaces lie within a fractured and cataclastic matrix, with short off-fault tensile fractures at high angles to the slip surfaces filled with the same material as the main slip surfaces (Figure 17D). At high resolution, the iron-rich slip zone material appears amorphous with a finely laminated appearance and small rounded fragments in the material (Figure 17D). The iron-rich material in the fault surfaces does not exhibit clear grain boundaries, suggesting the material may have a melt origin.

The thin slip surfaces (Figure 17) provide a quantification of the alteration in these faulted rocks and a calibration between the XRF maps and iron concentrations. The whole rock analysis

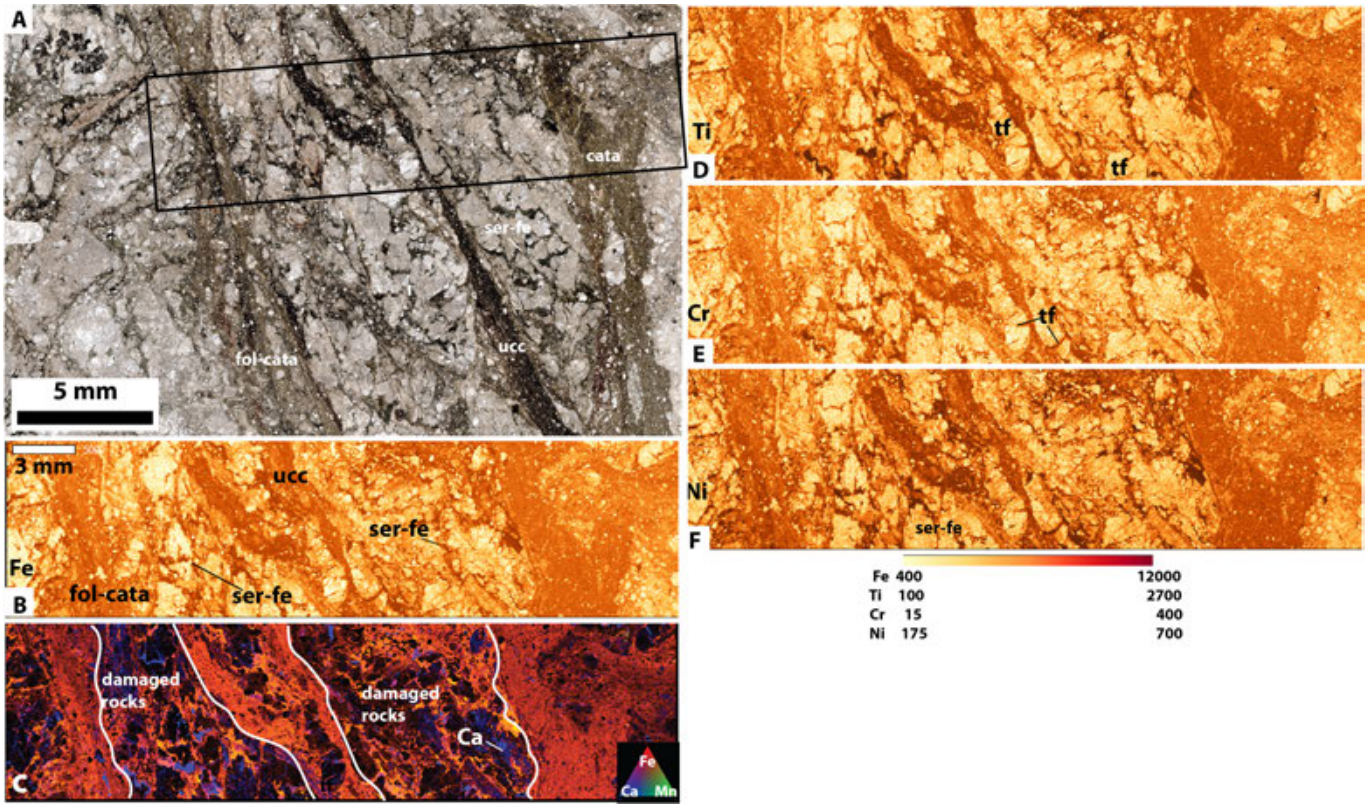

Figure 15 – Microstructures and elemental distribution in sample LE 6-433 of the San Andreas Fault damage zone- slip zone transition, Lake Elizabeth site. **A)** Plane-polarized light photomicrograph of a thin section (see Figures 2A and 3B for location). This sample represents a more mature fault development stage, transitioning from fractured damage zone rocks to cataclastically sheared fault-related rocks. The rectangle indicates the region examined with XRF mapping. The sample consists of elongate damage zone rocks dominated by plagioclase, three cataclastic zones, and a thin slip surface marked by optically opaque materials. **B)** Elemental iron map of a portion of the sample. The sheared cataclasites (cata) are rich in Fe, Mn, Ti, Cr, and Ni –comprised of very fine-grained cataclasite and ultracataclasite (ucc). Serrated iron-enriched zones (ser-fe) are common in damaged rocks. In some zones, compositional layering is evident. **C)** Tricolor map of Fe (red), Mn (green), and Ca (blue) shows that iron dominates the cataclastic zones. Regions with slight orange tint indicate areas where Fe is mixed with Ti, Cr, and Ni. Calcium, likely as calcite, occurs as small irregular zones that are likely disarticulated calcite veins. The white lines define the edges of the damaged zones. The maps of metals **D) Ti**, **E)** Cr, and **F)** Ni mimic the Fe patterns. Fractures and sheared zones are irregular and connect to equant grains. Likely, magnetite grains (black) are altered, and Fe+Ti+Cr+Mn are distributed in irregular fractures associated with the magnetite. Fractures in the feldspars are lined with transition elements and define angular to subangular fragments.

for Sample 6-134 yields a total iron value of 5.24 wt% on a volatile-free basis. Detailed microprobe data from energy dispersive spectroscopy shows that the slip surfaces have 11-12 wt% Fe and the damage zones are between 7 and 9 wt% (Figure 17E, Supporting Information). These values represent local iron concentrations over twice that of traditional whole rock analysis, showing the mineralization heterogeneity in the deformed rocks.

Narrow slip surfaces exhibit shear fabrics (Figure 18) with extremely fine-grained, amorphous iron-rich fault fill defining sharp boundaries in a sample from the San Andreas Fault. Narrow slip surfaces cut well-defined protolith fabrics. Within the fine-grained cataclasite matrix, irregular, elongate, and folded zones of light element concentrations (Figure 18C) are distributed throughout. Some of these are enriched in potassium (figure 18D), and the lack of any other elemental signature suggests these zones are likely enriched in sodium, which is below the detection limit for the beamlines.

In the San Gabriel Fault, extremely narrow slip surfaces are marked by iron concentrations in fine-grained clay-zeolite-carbonate-rich sheared rocks (Figure 19). The highly sheared, foliated clays, carbonates, zeolites, and iron oxides are brecciated and cut by 5-20 μm thick surfaces defined by concentrations of iron and related metal cations (Figure 19B). The nature of these dark surfaces suggests that these might result from a superposed pressure solution on the shearing and brecciation. Early-formed foliation defined by calcium distrusted in irregular blebs within iron-rich folia are cut by later sheared zones and by the development of a second foliation (Figure 19C). Correlations amongst Mn, Cr, and Ni in several of the samples examined here (Figures SI-2-4, Supporting Information), and thus the Cr signature in the trace element data is a proxy for the effects of Mn and the mobility of other transition elements such as V, Co, Cu, and Zn.

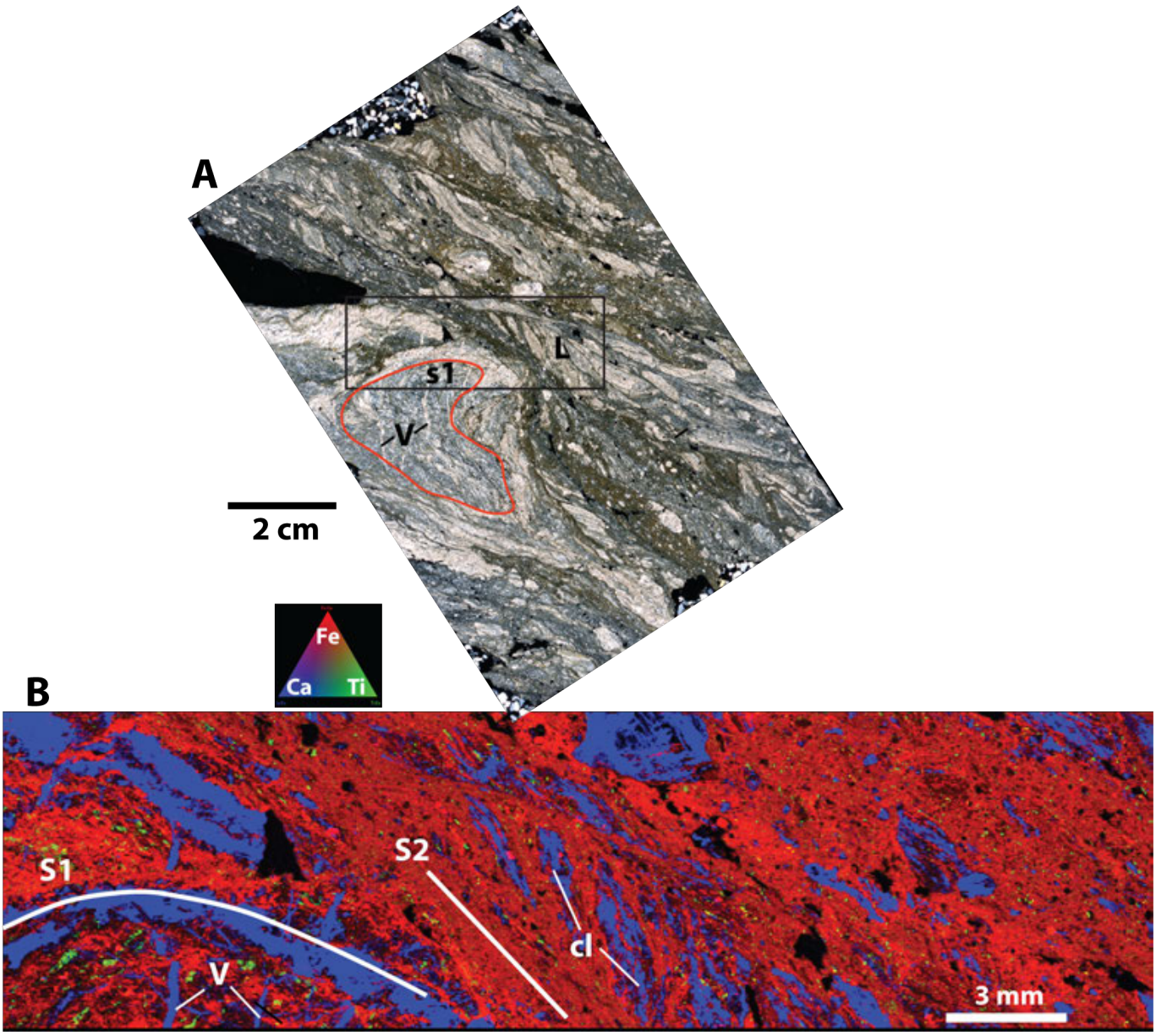

Figure 16 – Microstructures and elemental distribution in sample SGF 65A from the San Gabriel Fault – a sample from the upper strand of the San Gabriel Fault slip zone. **A)** Plane-polarized light photomicrograph of the sample (see Figures 2B and 3G for location). The rectangle indicates the region examined with XRF mapping. The sample shows the nature of highly sheared calcite and zeolite mineralized zones. Calcite lozenges (L) are distributed en-echelon within fine-grained foliated cataclasite define foliation with folded/rolled veins outlined by dashed white lines. Light regions are Ca-rich zones bounded by slip surfaces (ss). **B)** Tricolored elemental map for the detailed region. Iron (red) and Mn are distributed in the fine-grained sheared rocks. Ti (green) occurs as specks in fine-grained sheared rocks. Ca is concentrated in elongated lozenges in the sheared rocks and as short, thin planar sites as veins (V). The large, rounded region is a rootless fold (red line – foliations S1) consisting of a calcite-rich rim and a fine-grained matrix of cataclasite and possibly zeolites, which are themselves cut by thin, straight calcite veins. Calcium-rich rounded-to-elongate zones are entrained in the fine-grained Fe-rich cataclasite. The later sheared fabric S2 separates these carbonate-zeolite zones.

6 Discussion and Implications

The optical microscopy, X-ray diffraction mineralogy, whole-rock chemistry, and X-ray elemental mapping results presented here indicate that the fault-related rocks in the shallow parts of the San Andreas and San Gabriel Faults experienced significant amounts of alteration and mineralization during deformation. *Crouch and Evans* (2023); *Studnicky* (2021), and the XRF-based maps presented here provide macroscopic and microscopic observations of fault-related rocks from shallow levels of an active segment of the San Andreas Fault and an exhumed, deeper part of the San Gabriel Fault. Both fault zones are composed of broad damage zones formed of fractured, faulted, and veined protoliths, within which fault zones 10 cm to several m thick exhibit the results of a large amount of shearing. These sheared rocks comprise fine-grained, finely foliated clay-rich gouge, cataclasites, and ultracataclasites. The mineralogic data (*Crouch and Evans*, 2023; *Evans and Chester*, 1995; *Studnicky*, 2021; *Williams et al.*,

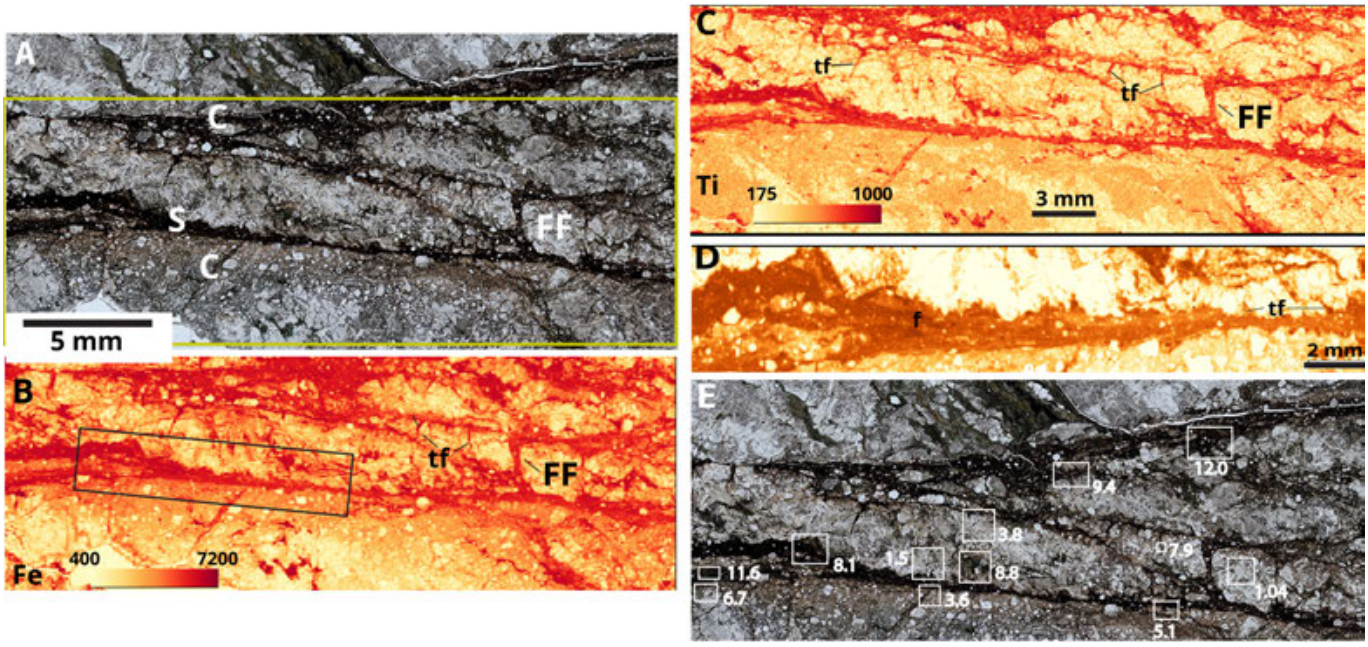

Figure 17 – Microstructures and elemental distribution in sample LE 6-134 of the San Andreas Fault damage zone, Lake Elizabeth site. **A)** Plane-polarized light photomicrograph of the sample (see Figure 2A for location). The rectangle indicates the region examined with XRF mapping in (B) and (C). The sample contains 50 mm to 1 mm thick black, optically opaque slip surfaces (S) and within cataclastic zones (C). The central zone is bounded by a straight boundary on one edge and an irregular wavy contact above. Filled fractures (FF) with sharp boundaries formed at high angles to the slip surfaces in several places. **B)** XRF map of iron distribution in the sample. The thin, filled fractures emanating from the main slip surfaces resemble off-fault tensile fractures (tf). The rectangular box indicates the region with a high-resolution map in (D). The darkest areas with count values of 7200 cps or higher correspond to total iron concentrations as high as 12 wt% (see E). **C)** Elemental maps for Ti reveal fine-scale texture within the sample. **D)** High-resolution magnified image of part of the lower slip surface. These data were processed with a 3-pixel window moving average to reduce image pixelation. The slip zone exhibits amorphous, foliated Fe (f) in the ~50 to 500 mm thick zone. Rounded fragments 10-50 μm of host cataclasite are suspended in the Fe-rich material. Minor wedge-shaped tensile fractures (tf) appear to have been injected (I) into the adjacent damaged rocks and cataclasite. **E)** Plane-polarized image of the sample with regions of EDS analyses (*Studnicky*, 2021) and the values of total iron analyses from the regions (Supporting Information). Iron is as high as 12.1% in the fault zones and ~1% in the protolith.

2021) document the presence of clay minerals, including Mg-bearing clays, chlorite-group minerals, calcite, zeolites, and iron oxide in the alteration assemblages.

The whole-rock geochemical data (Figures 7-10) along with the optical microscopy (Figures 5 and 6; see also *Crouch and Evans*, 2023; *Studnicky*, 2021; *Williams et al.*, 2021) provide mm- to the cm-scale resolution of the fault-related damage zone and fault zone rocks that are mixtures of altered protoliths (Figures 8 and 9; see also *Williams et al.*, 2021), where Fe, Ca, Mg, and loss on ignition components are enriched, to varying degrees in the deformed rocks. Loss on ignition values as high as 6%, compared with protolith values of sim1-2%, is most likely a measure of the effects of H_2O and CO_2-bearing fluids that interacted with the fault zones, either by alteration reactions or by the minerals added to the rocks via the formation of veins and fracture-filling. These values indicate higher fluid flux within the fault core and damage zone than in the surrounding protolith, resulting in fluid-rock interaction and mineral alteration.

The rare-earth and trace-element chemistry further indicates syntectonic alteration and mineralization in both fault zones. Large-ion enrichment is often related to alteration and hydrothermal alteration (e.g., *Rumbiak et al.*, 2021), where the Cs enrichment may be the consequence of 1) K- and Na-Ca bearing feldspar alteration and the subsequent development of clays, 2) the formation of zeolites, deposition of calcite, alteration of hornblende and biotite, the transition of iron oxides to chloritic minerals, and 3) the migration of transition metals in the deformed rocks. Cesium enrichments may be related to fluid fluxes through protolith granodiorites and into fault damage zones (*Mathurin et al.*, 2014; *Eveliina et al.*, 2016). The V and Cr enrichment (and by association, Fe, Ni, Ti, Zn, and Mn examined in the XRF maps) suggests transport, likely in the reduced state of these elements, and subsequent deposition in oxic conditions. These signatures are consistent with the presence of manganese (0.1-0.2 wt% of the amphibolite gneiss and the quartzo-feldspathic gneisses; see data tables here: Table 1 and Table 2) associated with Fe in the deformed rocks (Figures 13-18 and Figures SI-2 to SI-4, Supporting Information). Owing to its valence state, MnO_2 is an effective "scavenger" of associated transition elements (*Jenne*, 1968; *Nicholson and Eley*, 1997). The high-field strength Th enrichment may

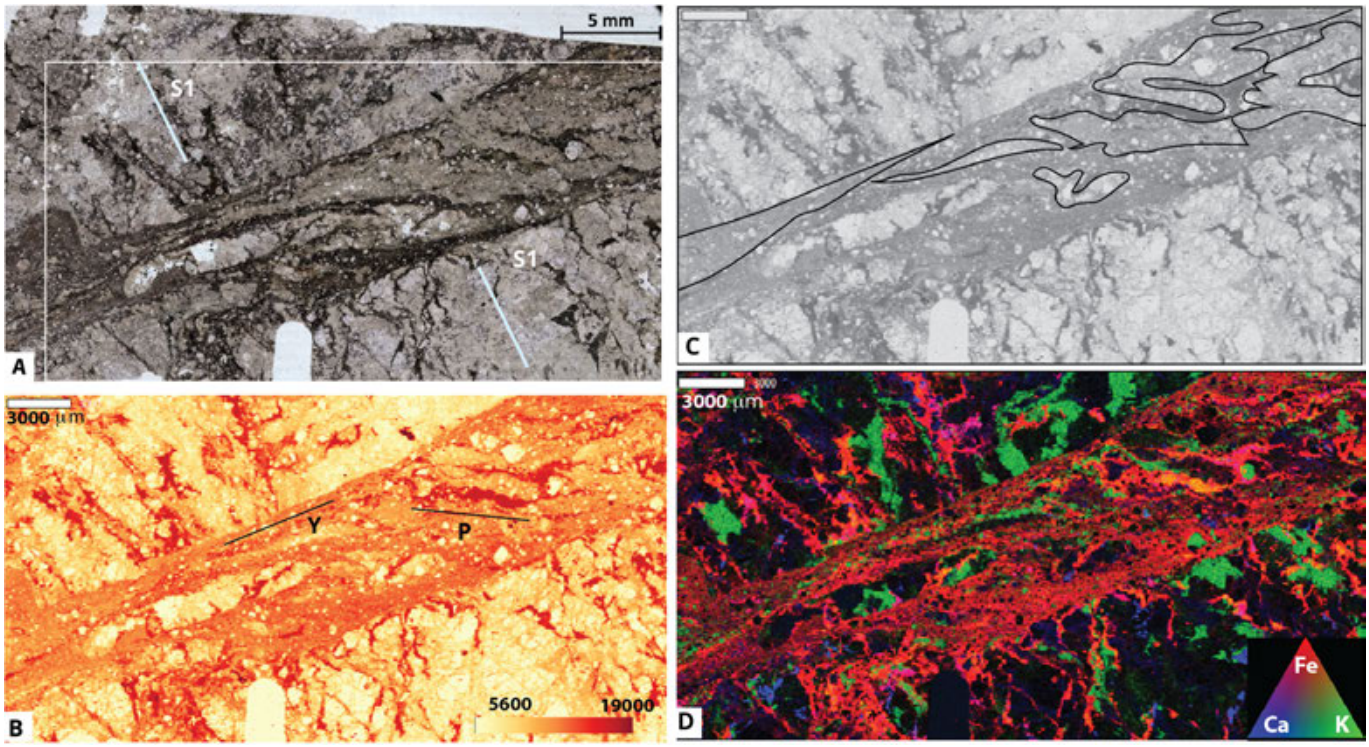

Figure 18 – Microstructures and elemental distribution in a magnified part of an ~0.5-1 cm wide fault zone sample from LE 4-130 of the San Andreas Fault sequence. **A)** Plane-polarized light photomicrograph of the sample with primary foliations (S1) cut by a zone of narrow shear surfaces. The rectangle shows the area examined in the XRF map. **B)** The foliated cataclasite sample consists of amorphous Fe-rich with rounded calcium and potassium-rich clasts. The iron-rich fractures below the fault are cut, and some of the iron is entrained in the fault; small, rounded clasts of feldspar lie in the fault zone. The sample exhibits a crude Riedel shear geometry, with a Y-P- and fabric indicating a top to the left sense of shear. **C)** Gray-scale map to show the elemental variations within the slip zone. Irregular and rootless folded light zones, likely enriched in light elements below our detection window (Na) line in dark Fe-Mn rich sheared zones. **D)** Tri-color Fe (red), K (green), and Ca (blue) plot of the shear zone. Primary K-rich zones in the protolith are K-feldspars elongated and distributed within the shear zone. Calcium occurs as small spots in the sheared zone. The shear zone is also enriched in Ti, Cr, and Mn. Remnant clasts of Ca-rich protolith (blue and green) parallel the S fabric, and a secondary fabric dips more steeply. Irregular iron-rich zones in the fault zone of higher concentrations are derived from altered and deformed mafic minerals, similar to the Fe-rich zones below the fault.

reflect hydrothermal processes (though there is debate regarding the immobile vs mobile nature of high-field strength elements (see *Jiang et al.*, 2005). Thorium enrichment may reflect volume loss, as U/Th values are lower in the deformed rocks; Th enrichments may also result from U decay to Th, as U is a trace element in calcite.

The degree and nature of synfaulting alteration documented by the whole-rock and optical microscopy for the San Andreas Fault samples are like those reported by *Williams et al.* (2021), *Ostermeijer et al.* (2022), and *Aben et al.* (in press). The moderate degree of alteration and mineralization observed at the optical and whole-rock scales consists of clay development from the alteration of feldspars, biotite, and hornblende, carbonate mineralization, and formation of zeolites. Cross-cutting relationships (*Williams et al.*, 2021; *Studnicky*, 2021) indicate that the San Andreas Fault zone at Lake Elizabeth experienced a history of alteration, mineralization, slip localization at the mm and finer scales, and distributed shearing over the mm to cm scales. The San Gabriel samples examined here provide evidence for moderate temperature alteration, mineralization, and deformation, consistent with the previous studies of the most deeply exhumed rocks from the fault (*Chester et al.*, 1993; *Evans and Chester*, 1995; *Crouch and Evans*, 2023).

Micron- to mm-scale XRF analyses of textures and elemental distribution further define the relationships between fine-scale mineralization and deformation. The Fe, Mn, ± Ti, Cr, or Ni mineralization occurred in fracture networks and the narrow fault zones (Figures 3, 11, and 12). Foliated cataclasites (Figures 13, 15, and 18) and the filling of intragranular fractures in the damaged host rock (Figure 12) are enriched in transition elements by up to a factor of 12. These metals, mobile in their reduced states, are mapped in rocks with slight deformation over 10 cm (Figure 11) down to the grain scales (Figure 12-19) and are a common feature of highly sheared rocks. In the San Andreas Fault examples, calcite and zeolite mineralization accompanied the fluid-rock interactions. We posit that hydrothermal fluids that moved through the host and the fractured rocks picked up these major, minor, and trace elements from the amphibole, biotite, and trace minerals such as rutile and

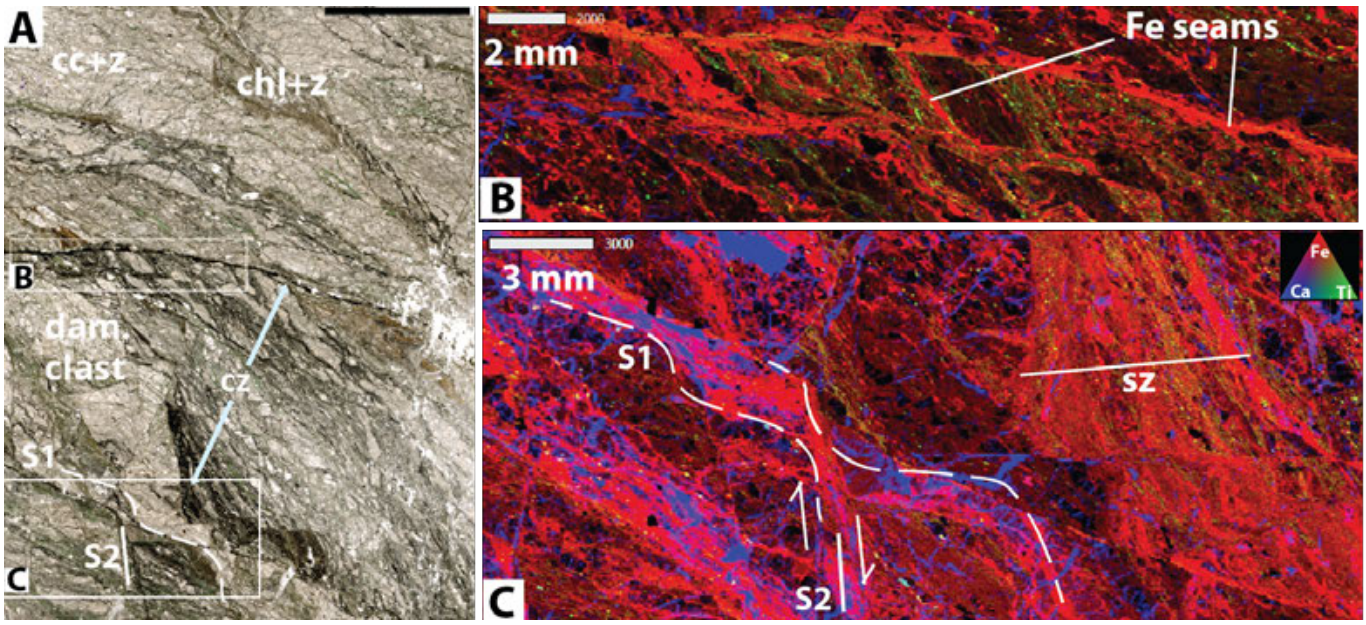

Figure 19 – Sample SGF 96.1 from the lower San Gabriel Fault zone encountered in the core. See Figures 2B and 3I for the location of this sample. **A)** Plane-polarized light photomicrograph of the sample. The rectangles indicate the region examined with XRF mapping. The sheared rock consists of zeolite + clays (Cl+Z) and calcite and zeolites (cc+z) and dark iron-rich zones that define the foliation (S1) and may define pressure solution seams. The clay + zeolite ± chlorite-rich foliated rocks are cut by cataclastic zones (cz), in which elongate fragments of the earlier sheared rocks lie in a dark fine-grained matrix of iron-rock cataclasite. **B)** XRF Fe map of the sheared rock. Fe-defined seams (Fe seams) 100-200 μm thick separate the elongated lozenges at the edge of the cataclasite zone. Very fine green specks indicate the distribution of Ti in the very fine-grained material. **C)** Early foliation S1, denoted by the dashed white lines, is offset by later S2 foliation and thin shear zone (sz). Ti is distributed through the sheared rocks, and Ca is disseminated in the rocks in irregular blebs in the earlier sheared fabric.

titanite and distributed them in multiscale networks. Carbonate mineralization occurred as the faults evolved (Figures 13-16), and the fault zones record these alteration processes. Slip localization onto highly foliated phyllosilicate zones occurred in the altered damage zones (Figures 17 and 18), and highly deformed rocks in the inner damage zones indicate a range of shear and possibly plastic processes, including folding of carbonates ± zeolite ± Fe-Mn-Mg oxide zones (Figures 6, 14, and 16).

Hydrothermal fluid-rock interactions that facilitate alteration and mineralization in fault zones (cf., *Callahan et al.*, 2020) produce alteration assemblages epidote calcite + laumontite. These assemblages indicate temperatures ≤ 250°C (*Utada*, 2001; *Ferrill et al.*, 2004, Figure 20), 100°C or more, greater than the likely ambient conditions for the fault-related rocks at either site (Figure 20). Laumontite is common along and within the San Andreas Fault and its exhumed predecessors, is stable within the temperature range of ~50 – 230°C (*Utada*, 2001), and appears in many parts of faults from the San Andreas Fault system (*Silver and James*, 1988; *Blenkinsop and Sibson*, 1992; *Evans and Chester*, 1995; *Wechsler et al.*, 2011; *Forand et al.*, 2018; *Crouch and Evans*, 2023). Calcite veins and cement are evidence of fluid-assisted healing within the fault damage zone.

Moderately indurated zones of Fe- and Mn-rich chloritic, clay, and zeolites formed early in the history of fault slip (*Studnicky*, 2021; *Williams et al.*, 2021) and were reworked in the fault zones as slip evolved. Mineralization and alteration are associated with fracture systems observed at the ~10 m scale (AMEC FosterWheeler Plate 7, LADWP; CHSRA report) to the sub-millimeter scales. These fractures facilitated fluid migration into the rocks and subsequent alteration and mineralization, which led to the generation of low-frictional and bulk elastic strength rocks.

The data presented here and the work of others on the San Andreas Fault (*Aben et al.*, in press; *Anderson et al.*, 1983; *Bradbury et al.*, 2015; *Chester et al.*, 1993; *Forand et al.*, 2018; *Gratier et al.*, 2011; *Holdsworth et al.*, 2011; *Moore and Rymer*, 2012; *Richard et al.*, 2014; *Schulz and Evans*, 2000; *Williams et al.*, 2021) and other faults (*Boulton et al.*, 2017; *Callahan et al.*, 2020; *Faulkner et al.*, 2003; *Holdsworth et al.*, 2011; *Jefferies et al.*, 2006; *Kaduri et al.*, 2017; *Niemeijer et al.*, 2012; *Smith et al.*, 2013; *Townend*, 2017; *Wibberley et al.*, 2008) indicate that complex combinations of deformation and geochemical processes strongly influence seismogenic faults. Deformation processes documented in our study include early-stage brittle fracture network development, gouge and cataclasite development, and pulverization (*Williams et al.*, 2021).

The data we present on the nature of hydrothermal alteration, mineralization, and deformation in these faults may help inform analyses of fault weakening and healing. Our Early-stage brittle fracture and faulting tend to increase the surface area of minerals available to mobile fluids to react,

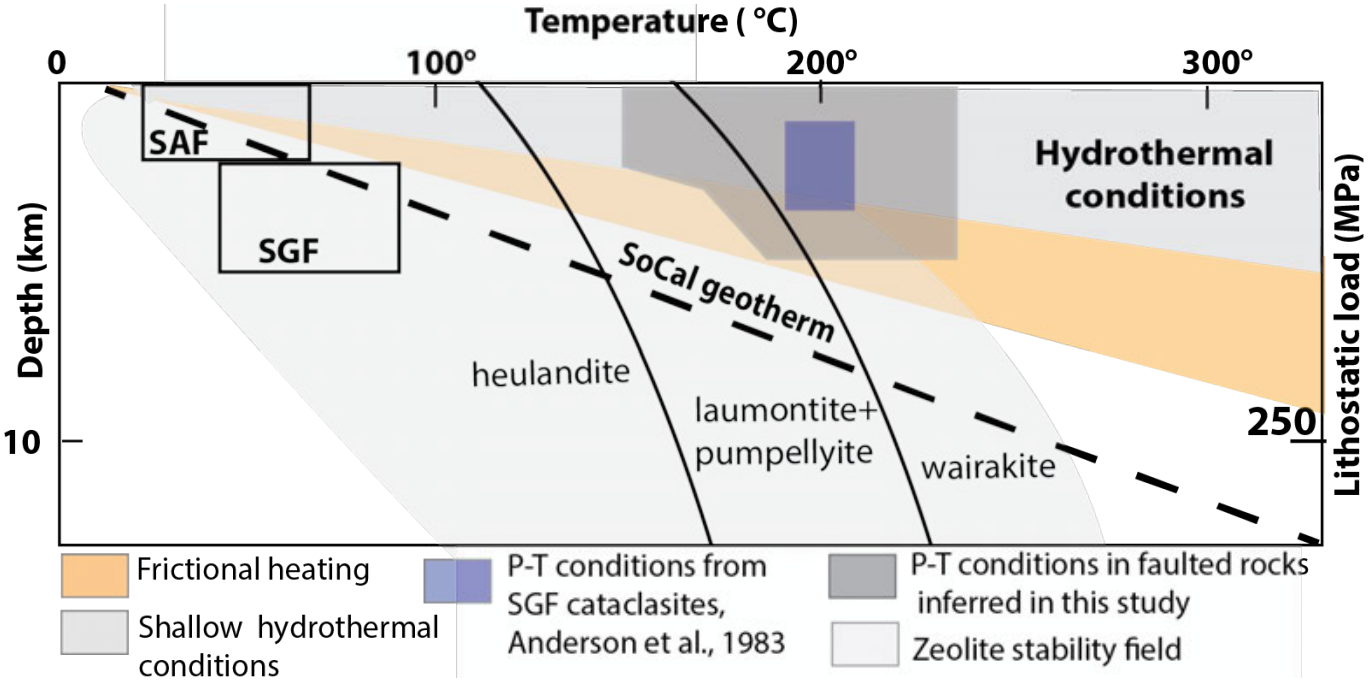

Figure 20 – This paper examines a conceptual model for conditions in and around the shallow San Andreas and San Gabriel fault zones. The rectangles labeled SAF and SGF are the likely ambient P-T conditions with geotherm P-T conditions when these rocks formed (present for SAF: 4-8 Mya for the SGF). The shaded dark gray region indicates the likely conditions for the assemblages in the cored samples from the San Andreas and San Gabriel faults based on the mineral assemblages, elemental distributions, and textures of the rocks. The dark blue area shows the P-T conditions and stability field adapted from *Anderson et al.* (1983), *Evans* (1988), and *Evans and Chester* (1995) for the San Gabriel fault-related rocks examined in surface exposures. The zeolite fields are adapted from *Weisenberger and Bucher* (2010) and *Utada* (2001). The hydrothermal alteration field represents the conditions under which free fluid phases could migrate in fractured and faulted crystalline rocks in the upper crust, and fluids would be at least partially oxidizing. In this region, fluids can transport heat and solutes. The SoCal geotherm is from *Lachenbruch* (1986) and *Buscher and Spotila* (2007). The zone of fault-related frictional heating indicates the likely range of temperatures based on frictional heating calculations of *Turcotte et al.* (1980) and *Lachenbruch* (1986) for a range of friction coefficients. Low-temperature zeolite phases are stable in these conditions, but laumontite, wairakite, and epidote are unstable. Fault-related mineral assemblages documented here and in *Anderson et al.* (1983) and *Evans* (1988) are consistent with externally derived hydrothermal fluids and fault-related heating and deformation that produce mineralization in the shallow portions of the faults.

promoting alteration and mineralization along fracture surfaces. With increased alteration to clay/phyllosilicate-rich fault rocks (cf. *Chester et al.*, 1993; *Faulkner et al.*, 2010; *Boulton et al.*, 2017), fault weakening would likely result. During the post-slip phase of the fault cycle, subsequent precipitation of veins and cement decreases the fault zone permeability. It could increase its strength and result in at least partial recovery, which is required in paradigmatic seismic cycle models (*Scholz*, 2019). The fault-related rocks in the San Andreas and San Gabriel faults exhibit evidence for inter-and intragranular cementation, primarily via carbonate and zeolite formation; carbonate and transitional elements fracture filling mineralization; pressure solution, and neocrystallization, especially of phyllosilicates. These observations may help guide further studies of fault healing in quartz-feldspathic protoliths *Blanpied et al.* (1995); *Niemeijer et al.* (2016); *Jeppson et al.* (2023), the nature of phyllosilicate recovery (*Shreedharan et al.*, 2023), cementations (*Tenthorey and Cox*, 2006), and pressure solution transformation (*Gratier et al.*, 2011). These processes may lead to the development of the cohesive, indurated rocks sampled by coring, such as those presented in this work.

7 Conclusions

Geochemical, microstructural, and elemental map data of deformed rocks from the San Andreas and San Gabriel Fault zones indicate that the faults experienced significant hydrothermal alteration and mineralization synchronous with brittle deformation at > 1 km to -4 km depth. Early fracture development was followed by fluid-transport-enabled alteration, resulting in zeolites + calcite + clays + chlorite ± hydrous phyllosilicates ± epidote. Fluid-assisted elemental concentrations in brittle and semi-brittle deformed random-fabric cataclasites, foliated cataclasites, phyllonite, and ultracataclasite shear zones accompanied fracture networks and minor faults in damaged zones. Fault damage zones up to 300 m thick consist of rocks significantly weaker at the grain- to meter-scale relative to the host rocks, with abundant microfractures and mesoscopic shear surfaces.

The fault-related alteration within the damage zone indicates a temperature regime of up to ~250°C,

a fault zone of reduced strength, with an at times open, permeable fracture system facilitating the fluid flow and element mobility, reduced permeability within gouge, and high concentration of low-seismic velocity minerals. The high degree of induration and lack of 'incohesive' fault-related rocks in these rocks may be due to the distribution of calcite and zeolite cement and veins, the development of fine-grained clay and the formation of Fe-Mg oxide sealed fractures, facilitated by the development of fracture networks that created fluid pathways in the fault zone. The brittle fractures increased the surface area of minerals available to mobile fluids to react, promoting alteration and mineralization. Although these mechanisms lead to fault weakening, the subsequent precipitation of veins and cement decreases the fault zone permeability and increases its strength.

Hydrothermal alteration at these shallow levels suggests the damaged zones experienced the advection of hydrothermal fluids or the in situ heating of fluids from the frictional heating within the fault zones. These processes produced shallow damage zones that may be significantly weaker than the protolith during some stages of the fault cycle and produced many potential slip surfaces during and after a major earthquake. Over time, mineralization may partially heal the fault-related rocks, creating intermediate-strength fault zones and influencing slip accommodation in the shallow crust.

Acknowledgements

We thank Dr. Kate Scharer of the U. S. Geological Survey for alerting us to the LADWP and CHRSA site investigations and introducing the scientific community to these valuable data sets. This research was supported by the Southern California Earthquake Center (SCEC) (Contribution #13451). SCEC is funded by NSF Cooperative Agreement EAR-1600087 and USGS Cooperative Agreement G20AC00070 fund SCEC. This work was also funded by an NSF grant 1824852, by the Geological Society of America - Continental Scientific Drilling Division Grants to Crouch and Studnicky, an American Association of Petroleum Geologists L. Austin Weeks grant, a Utah State University's Academic Opportunity grant, URCO grant, Peak Summer Research Fellowship, and a College of Science mini-grant to Kaitlyn Crouch; Caroline Studnicky was supported by the Geological Society of America - Graduate Student Research Grant 2020; a Utah State University - J. Stewart Williams Graduate Fellowship Spring 2019; Utah State University - Summit Scholarship Spring 2020; and an Association of Women Geologists - Salt Lake Chapter Research Grant 2019. Microscopy that guided the XRF mapping of the San Andreas Fault was performed at McGill University with the guidance of Dr. Christie Rowe and Dr. Jamie Kirkpatrick with funding from Fonds de Recherche du Québec, Bourses d'Excellence Pour Étudiants Étrangers Assistance. Chris Heron of the Los Angeles Department of Water and Power provided access to the SAF drill core and borehole log data. Thanks to Dr. Christie Rowe and Dr. Randy Williams for discussing this work. Access to the CHSRA core was provided by Kathlien Red (Kleinfelder) and Randy Anderson (CHSRA) in 2019 and by Kleinfelder staff in 2018. Paul Guptill (Kleinfelder) and the California High-Speed Rail Authority provided access to borehole data from the borehole released under the California High-Speed Rail Public Records request #22-164, October 2022, via the CHSRA Public Records Act portal. Use of the Stanford Synchrotron Radiation Lightsource, SLAC National Accelerator Laboratory, is supported by the U.S. Department of Energy, Office of Science, Office of Basic Energy Sciences under Contract No. DE-AC02-76SF00515. The SSRL Structural Molecular Biology Program is supported by the DOE Office of Biological and Environmental Research, the National Institutes of Health, and the National Institute of General Medical Sciences (P30GM133894). The contents of this publication are solely the responsibility of the authors and do not necessarily represent the official views of the NIGMS, NIH, DOE, or SLAC. Many thanks to the journal reviewers and editors who provide insightful comments and edits to an earlier version of this paper.

Author contributions

Kaitlyn Crouch, Caroline Studnicky, and James Evans sampled the core in 2017, 2018, and 2019. **Crouch and Studnicky** examined the drill core in detail, recompiled the fracture spacing and borehole data from the geotechnical data sets, performed microstructural studies that guided the geochemical studies, completed the X-ray diffraction studies, and compiled and curated all the data sets, including optical microscopy images of the core samples. **Crouch and Evans** performed the XRF analyses of San Gabriel and San Andreas samples at SSRL in collaboration with **Sharon Bone and Sam Webb** in February 2020, and **Sharon Bone** examined San Gabriel samples via remote protocols in the autumn of 2020 in cooperation with **Crouch and Evans**. **Evans, Bone, Edwards, and Webb** performed the XRF analyses of San Andreas samples in 2018, and **Evans, Edwards, and Webb** mapped all the core samples. **Evans and Crouch** reduced the data with the MicroAnalysis Toolkit software (https://www.sams-xrays.com/smak) developed by Samuel Webb at the Stanford Linear Accelerator Center (SLAC). **Evans** conceived of and primarily designed the core-based studies and the analyses of the samples with XRF mapping methods and wrote this paper, based on MSc. theses by **Kaitlyn Crouch** and **Caroline Studnicky**, with edits, comments, and revisions from co-authors.

Data availability

The original thin section photomicrographs, SEM images, and images from microprobe analyses are available from: https://digitalcommons.usu.edu/all_datasets/142/ for the San Andreas Fault, and https://digitalcommons.usu.edu/all_datasets/193/ for the San Gabriel Fault. The whole-rock geochemical and microprobe data, and the results of their analyses, are available at:

- https://works.bepress.com/james_evans/154/
- https://works.bepress.com/james_evans/155/
- https://works.bepress.com/james_evans/156/

The raw files for the X-Ray fluorescence map data acquired at the SSRL can be requested from the senior author. The raw data are .HDFS files that can be manipulated with appropriate software such as SMAK (https://www.sams-xrays.com/smak; *Webb*, 2011).

Competing interests

The authors declare no competing interests.

Peer review

This publication was peer-reviewed by Lydia Baily, Tsuyoshi Ishikawa, and Simone Masoch. The full peer-review report can be found here: tektonika.online/index.php/home/article/view/47/95

Copyright notice

References

Aben, F. M., K. Farrington, B. G. M. Boris Galvan Sanchez, T. M., S. A. Miller, T. K. Rockwell, H. Girty, G. H., G. Ostermeijer, and N. Wechsler (in press), Chemically altered Pulverized granite along the Mojave section of the SAF shows evidence for large-scale heat transfer by post-seismic fluid flow and fluid overpressure at depth, Geochemistry, Geophysics, and Geosystems, *Geochemistry, geophysics, geosystems: G(3)*.

Anderson, J. L., R. H. Osborne, and D. F. Palmer (1983), Cataclastic rocks of the San Gabriel fault—an expression of deformation at deeper crustal levels in the San Andreas fault zone, *Tectonophysics*, *98*, 209–251, doi: 10.1016/0040-1951(83)90296-2.

Archuleta, R. J. (1984), A faulting model for the 1979 Imperial Valley earthquake, *Journal of geophysical research*, *89*(B6), 4559–4585, doi: 10.1029/jb089ib06p04559.

Barth, A. P., J. L. Wooden, R. M. Tosdal, and J. Morrison (1995a), Crustal contamination in the petrogenesis of a calc-alkalic rock series: Josephine Mountain intrusion, California, *Geological Society of America Bulletin*, *107*(2), 201–212, doi: 10.1130/0016.

Barth, A. P., J. L. Wooden, R. M. Tosda, J. Morrison, and others (1995b), Origin of gneisses in the aureole of the San Gabriel anorthosite complex and implications for the Proterozoic crustal evolution of southern California, *Tectonics*, *14*, 736–752, doi: 10.1130/0016-7606(1995)107.

Bemis, S. P., K. Scharer, and J. F. Dolan (2021), The San Andreas Fault Paleoseismic Record at Elizabeth Lake: Why are There Fewer Surface-Rupturing Earthquakes on the Mojave Section?, *Bulletin of the Seismological Society of America*, *111*(3), 1590–1613, doi: 10.1785/0120200218.

Bergmann, U., L. Bertrand, N. P. Edwards, P. L. Manning, and R. A. Wogelius (2020), Chemical Mapping of Ancient Artifacts and Fossils with X-Ray Spectroscopy, in *Synchrotron Light Sources and Free-Electron Lasers: Accelerator Physics, Instrumentation and Science Applications*, edited by E. J. Jaeschke, S. Khan, J. R. Schneider, and J. B. Hastings, pp. 2393–2455, Springer International Publishing, Cham, doi: 10.1007/978-3-030-23201-6_77.

Beyer, L. A., T. H. McCulloh, R. E. Denison, R. W. Morin, R. J. Enrico, J. A. Barron, and R. J. Fleck (2009), *Post-Miocene right separation on the San Gabriel and Vasquez Creek faults, with supporting chronostratigraphy, western San Gabriel Mountains*, 27 pp., U.S. Geological Survey Professional Paper, California.

Blanpied, M. L., D. A. Lockner, and J. D. Byerlee (1995), Frictional slip of granite at hydrothermal conditions, *Journal of geophysical research*, *100*(B7), 13,045–13,064, doi: 10.1029/95jb00862.

Blenkinsop, T. G., and R. H. Sibson (1992), Aseismic fracturing and cataclasis involving reaction softening within core material from the Cajon Pass Drill Hole, *Journal of geophysical research*, *97*(B4), 5135–5144, doi: 10.1029/90jb02285.

Blythe, A. E., M. A. House, and J. A. Spotila (2002), Low-temperature thermochronology of the San Gabriel and San Bernardino Mountains, southern California: Constraining structural evolution, in *Contributions to Crustal Evolution of the Southwestern United States*, vol. 365, edited by A. Barth, pp. 231–250,, Geological Society of America, Boulder, Colorado, doi: 10.1130/0-8137-2365-5.231.

Boulton, C., C. D. Menzies, V. G. Toy, J. Townend, and R. Sutherland (2017), Geochemical and microstructural evidence for interseismic changes in fault zone permeability and strength, Alpine Fault, *New Zealand, Geochemistry, Geophysics, Geosystems*, *18*, 238–265,, doi: 10.1002/2016GC006588.

Bradbury, K. K., J. P. Evans, J. S. Chester, F. M. Chester, and D. L. Kirschner (2011), Lithology and internal structure of the San Andreas fault at depth based on characterization of Phase 3 whole-rock core in the San Andreas Fault Observatory at Depth (SAFOD) borehole, *Earth and planetary science letters*, *310*(1-2), 131–144, doi: 10.1016/j.epsl.2011.07.020.

Bradbury, K. K., C. R. Davis, J. W. Shervais, S. U. Janecke, and J. P. Evans (2015), Composition, alteration, and texture of fault-related rocks from SAFOD core and surface outcrop analogs: Evidence for deformation processes

and fluid-rock interactions, *Pure and Applied Geophysics*, *172*, 1053–1078,, doi: 10.1007/s00024-014-0896-6.

Bruhn, R. L., W. T. Parry, W. A. Yonkee, and T. Thompson (1994), Fracturing and hydrothermal alteration in normal fault zones, *Pure and applied geophysics*, *142*(3-4), 609–644, doi: 10.1007/bf00876057.

Bryant, W. A., and Compiler (2017), Fault number 89c, San Gabriel fault zone, Newhall section, in Quaternary fault and fold database of the United States: U.S, *Geological Survey*.

Buscher, J. T., and J. A. Spotila (2007), Near-field response to transpression along the southern San Andreas fault, based on exhumation of the northern San Gabriel Mountains, southern California, *Tectonics*, *26*(5), doi: 10.1029/2006tc002017.

Callahan, O. A., P. Eichhubl, and N. C. Davatzes (2020), Mineral precipitation as a mechanism of fault core growth, *Journal of structural geology*, *140*(104156), 104,156, doi: 10.1016/j.jsg.2020.104156.

Chester, F., J. P. Evans, and R. Biegel (1993), Internal structure and weakening mechanisms of the San Andreas Fault, *Journal of geophysical research*, *98*, 771–786, doi: 10.1029/92JB01866.

Chester, F. M., and J. S. Chester (1998), Ultracataclasite structure and friction processes of the Punchbowl fault, San Andreas system, California, *Tectonophysics*, *295*(1), 199–221, doi: 10.1016/S0040-1951(98)00121-8.

Cochran, E. S., Y.-G. Li, P. M. Shearer, S. Barbot, Y. Fialko, and J. E. Vidale (2009), Seismic and geodetic evidence for extensive, long-lived fault damage zones, *Geology*, *37*(4), 315–318, doi: 10.1130/G25306A.1.

Cooperdock, E., and A. Ault (2020), Iron oxide (U–Th)/He thermochronology: New perspectives on faults, fluids, and heat, *Elements*, *16*, 319–324, doi: 10.2138/gselements.16.5.319.

Crouch, K., and J. Evans (2023), Shallow Composition and Structure of the Upper Part of the Exhumed San Gabriel Fault, California: Implications for Fault Processes, *τεκτονικα*, *1*(2), 76–100, doi: 10.55575/tektonika2023.1.2.30.

Crouch, K. A. (2022), Shallow composition and structure of the San Gabriel fault, California in drill core and geophysical logs: Implications for fault slip and energetics, *All Graduate Theses and Dissertations*, doi: 10.26076/A629-B091.

d'Alessio, M. A., A. Blythe, and R. Bürgmann (2003), No frictional heat along the San Gabriel fault, California: Evidence from fission-track thermochronology, *Geology*, *31*, 541–544, doi: 10.1130/0091-7613(2003)031<0541:NFHATS>2.0.CO;2.

Dibblee, T. W., Jr, and B. Carter (2002), Geologic Map of the Condor Peak Quadrangle.

Dolan, J. F., and B. D. Haravitch (2014), How well do surface slip measurements track slip at depth in large strike-slip earthquakes? The importance of fault structural maturity in controlling on-fault slip versus off-fault surface deformation, *Earth and planetary science letters*, *388*, 38–47, doi: 10.1016/j.epsl.2013.11.043.

Dor, O., Y. Ben-Zion, T. K. Rockwell, and J. Brune (2006), Pulverized rocks in the Mojave section of the San Andreas Fault Zone, *Earth and planetary science letters*, *245*(3-4), 642–654, doi: 10.1016/j.epsl.2006.03.034.

Dorsey, M. T., T. K. Rockwell, G. H. Girty, G. A. Ostermeijer, J. Browning, T. M. Mitchell, and J. M. Fletcher (2021), Evidence of hydrothermal fluid circulation driving elemental mass redistribution in an active fault zone, *Journal of structural geology*, *144*(104269), 104,269, doi: 10.1016/j.jsg.2020.104269.

Duan, Q., X. Yang, S. Ma, J. Chen, and J. Chen (2016), Fluid–rock interactions in seismic faults: Implications from the structures and mineralogical and geochemical compositions of drilling cores from the rupture of the 2008 Wenchuan earthquake, China, *Tectonophysics*, *666*, 260–280, doi: 10.1016/j.tecto.2015.11.008.

Edwards, N. P., S. M. Webb, C. M. Krest, D. van Campen, P. L. Manning, R. A. Wogelius, and U. Bergmann (2018), A new synchrotron rapid-scanning X-ray fluorescence (SRS-XRF) imaging station at SSRL beamline 6-2, *Journal of synchrotron radiation*, *25*(Pt 5), 1565–1573, doi: 10.1107/S1600577518010202.

Evans, J. P. (1988), Deformation mechanisms in granitic rocks at shallow crustal levels, *Journal of Structural Geology*, *10*(5), 437–443, doi: 10.1016/0191-8141(88)90031-4.

Evans, J. P., and F. M. Chester (1995), Fluid-rock interaction in faults of the San Andreas system: Inferences from San Gabriel fault rock geochemistry and microstructures, *Journal of geophysical research*, *100*(B7), 13,007–13,020, doi: 10.1029/94jb02625.

Eveliina, M., I. Jussi, M.-A. Minja, L. Antero, H. Stellan, V. Mikko, S.-K. Marja, and A. Martin (2016), Behavior of Cs in Grimsel granodiorite: sorption on main minerals and crushed rock, *Radiochimica Acta*, *104*, 575–582, doi: 10.1515/ract-2015-2574.

Farfan, G. A., A. Apprill, S. M. Webb, and C. M. Hansel (2018), Coupled X-ray Fluorescence and X-ray Absorption Spectroscopy for Microscale Imaging and Identification of Sulfur Species within Tissues and Skeletons of Scleractinian Corals, *Analytical chemistry*, *90*(21), 12,559–12,566, doi: 10.1021/acs.analchem.8b02638.

Faulkner, D. R., A. C. Lewis, and E. H. Rutter (2003), On the internal structure and mechanics of large strike-slip fault zones: field observations of the Carboneras fault in southeastern Spain, *Tectonophysics*, *367*(3-4), 235–251, doi: 10.1016/s0040-1951(03)00134-3.

Faulkner, D. R., C. A. L. Jackson, R. J. Lunn, R. W. Schlische, Z. K. Shipton, C. A. J. Wibberley, and M. O. Withjack (2010), A review of recent developments concerning the structure, mechanics and fluid flow properties of fault zones, *Journal of structural geology*, *32*(11), 1557–1575, doi: 10.1016/j.jsg.2010.06.009.

Ferrill, D. A., A. P. Morris, M. A. Evans, M. Burkhard, R. H. Groshong, Jr, and C. M. Onasch (2004), Calcite twin morphology: a low-temperature deformation geothermometer, *Journal of structural geology*, *26*(8), 1521–1529, doi: 10.1016/j.jsg.2003.11.028.

Field, E. H., R. J. Arrowsmith, G. P. Biasi, P. Bird, T. E. Dawson, K. R. Felzer, D. D. Jackson, K. M. Johnson, T. H. Jordan, C. Madden, A. J. Michael, K. R. Milner, M. T. Page, T. Parsons, P. M. Powers, B. E. Shaw, W. R. Thatcher, R. J. Weldon, and Y. Zeng (2014), Uniform California earthquake rupture forecast, version 3 (UCERF3)–the time-independent model, *Bulletin of the Seismological Society of America*, *104*(3), 1122–1180, doi: 10.1785/0120130164.

Forand, D., J. P. Evans, S. U. Janecke, and J. Jacobs (2018), Insights into fault processes and the geometry of the San

Andreas fault system: Analysis of core from the deep drill hole at Cajon Pass, California, *Geological Society of America bulletin*, *130*(1-2), 64–92, doi: 10.1130/b31681.1.

Fusseis, F., X. Xiao, C. Schrank, and F. De Carlo (2014), A brief guide to synchrotron radiation-based microtomography in (structural) geology and rock mechanics, *Journal of structural geology*, *65*, 1–16, doi: 10.1016/j.jsg.2014.02.005.

Gratier, J.-P., J. Richard, F. Renard, S. Mittempergher, M.-L. Doan, G. Di Toro, J. Hadizadeh, and A.-M. Boullier (2011), Aseismic sliding of active faults by pressure solution creep: Evidence from the San Andreas Fault Observatory at Depth, *Geology*, *39*(12), 1131–1134, doi: 10.1130/g32073.1.

Hauksson, E., and M.-A. Meier (2019), Applying depth distribution of seismicity to determine Thermo-mechanical properties of the seismogenic crust in southern California: Comparing lithotectonic blocks, *Pure and applied geophysics*, *176*(3), 1061–1081, doi: 10.1007/s00024-018-1981-z.

Hernandez, J. L. (2011), Preliminary Geologic Map of the Lake Hughes 7.5' Quadrangle.

Holdsworth, R. E., E. W. E. van Diggelen, C. J. Spiers, J. H. P. de Bresser, R. J. Walker, and L. Bowen (2011), Fault rocks from the SAFOD core samples: Implications for weakening at shallow depths along the San Andreas Fault, California, *Journal of structural geology*, *33*(2), 132–144, doi: 10.1016/j.jsg.2010.11.010.

Isaacs, A. J., J. P. Evans, P. T. Kolesar, and T. Nohara (2008), Composition, microstructures, and petrophysics of the Mozumi fault, Japan: In situ analyses of fault zone properties and structure in sedimentary rocks from shallow crustal levels, *Journal of geophysical research*, *113*(B12), doi: 10.1029/2007jb005314.

Jefferies, S. P., R. E. Holdsworth, C. A. J. Wibberley, T. Shimamoto, C. J. Spiers, A. R. Niemeijer, and G. E. Lloyd (2006), The nature and importance of phyllonite development in crustal-scale fault cores: an example from the Median Tectonic Line, Japan, *Journal of Structural Geology*, *28*(2), 220–235, doi: 10.1016/j.jsg.2005.10.008.

Jenne, E. (1968), Controls on Mn, Fe, co, Ni, cu, and Zn concentrations in soils and water: The significant role of hydrous Mn and Fe oxides, *Advances in inorganic chemistry*, pp. 337–387, doi: 10.1021/BA-1968-0073.CH021.

Jeppson, T. N., and H. J. Tobin (2015), San Andreas fault zone velocity structure at SAFOD at core, log, and seismic scales, *Journal of geophysical research. Solid earth*, *120*(7), 4983–4997, doi: 10.1002/2015jb012043.

Jeppson, T. N., K. K. Bradbury, and J. P. Evans (2010), Geophysical properties within the San Andreas Fault Zone at the San Andreas Fault Observatory at Depth and their relationships to rock properties and fault zone structure, *Journal of geophysical research*, *115*(B12), doi: 10.1029/2010jb007563.

Jeppson, T. N., D. A. Lockner, N. M. Beeler, and D. E. Moore (2023), Time-dependent weakening of granite at hydrothermal conditions, *Geophysical research letters*, *50*(21), 2023 105,517„ doi: 10.1029/2023gl105517.

Jiang, S.-Y., R.-C. Wang, X.-S. Xu, and K.-D. Zhao (2005), Mobility of high field strength elements (HFSE) in magmatic-, metamorphic-, and submarine-hydrothermal systems, *Physics and Chemistry of the Earth, Parts A/B/C*, *30*(17), 1020–1029, doi: 10.1016/j.pce.2004.11.004.

Kaduri, M., J.-P. Gratier, F. Renard, Z. Çakir, and C. Lasserre (2017), The implications of fault zone transformation on aseismic creep: Example of the North Anatolian Fault, Turkey, *Journal of geophysical research. Solid earth*, *122*(6), 4208–4236, doi: 10.1002/2016jb013803.

Kaneko, Y., and Y. Fialko (2011), Shallow slip deficit due to large strike-slip earthquakes in dynamic rupture simulations with elasto-plastic off-fault response, *Geophysical journal international*, *186*(3), 1389–1403, doi: 10.1111/j.1365-246x.2011.05117.x.

Kelly, S. D., D. Hesterberg, and B. Ravel (2008), Analysis of Soils and Minerals Using X-ray Absorption Spectroscopy, in *Methods of Soil Analysis Part 5—Mineralogical Methods, 5.5*, edited by A. L. Ulery and L. R. Drees, Soil Science Society of America.

Lachenbruch, A. H. (1986), Simple models for the estimation and measurement of frictional heating by an earthquake, *Tech. rep.*, US Geological Survey.

LADWP (2019), Final Report of San Andreas Coring Operation Near Elizabeth Lake Tunnel, California, *Tech. rep.*, Los Angeles Department of Water and Power (LADWP), California, doi: 10.17605/OSF.IO/2VN6X.

Lindvall, S., S. Kerwin, C. Heron, C. A. Davis, J. Tyson, J. Chestnut, K. Mass, M. Farr, K. Scharer, and D. McPhillips (2018), Characterizing the Los Angeles aqueduct crossing of the San Andreas fault for improved earthquake resilience, in *11th National Conference on Earthquake Engineering*.

Marchandon, M., J. Hollingsworth, and M. Radiguet (2021), Origin of the shallow slip deficit on a strike slip fault: Influence of elastic structure, topography, data coverage, and noise, *Earth and planetary science letters*, *554*(116696), 116,696, doi: 10.1016/j.epsl.2020.116696.

Marone, C., and D. M. Saffer (2007), *Fault Friction and the Upper Transition From Seismic to Aseismic Faulting, in The Seismogenic Zone of Subduction Thrust Faults*, 346–369, pp., Columbia University Press.

Marone, C., and C. H. Scholz (1988), The depth of seismic faulting and the upper transition from stable to unstable slip regimes, *Geophysical research letters*, *15*(6), 621–624, doi: 10.1029/gl015i006p00621.

Mathurin, F., H. Drake, E. Tullborg, T. Berger, P. Peltola, B. Kalinowski, and M. Åström (2014), High cesium concentrations in groundwater in the upper 1.2 km of fractured crystalline rock – Influence of groundwater origin and secondary minerals, *Geochimica et cosmochimica acta*, *132*, 187–213, doi: 10.1016/J.GCA.2014.02.001.

Mitchell, T. M., and D. R. Faulkner (2009), The nature and origin of off-fault damage surrounding strike-slip fault zones with a wide range of displacements: A field study from the Atacama fault system, northern Chile, *Journal of structural geology*, *31*(8), 802–816, doi: 10.1016/j.jsg.2009.05.002.

Moore, D. E., and M. J. Rymer (2012), Correlation of clayey gouge in a surface exposure of serpentinite in the San Andreas Fault with gouge from the San Andreas Fault Observatory at Depth (SAFOD), *Journal of structural geology*, *38*, 51–60, doi: 10.1016/j.jsg.2011.11.014.

Moser, A. C., J. P. Evans, A. K. Ault, S. U. Janecke, and K. K. Bradbury (2017), (U–Th)/He thermochronometry reveals Pleistocene punctuated deformation and

synkinematic hematite mineralization in the Mecca Hills, southernmost San Andreas Fault zone, *Earth and planetary science letters*, *476*, 87–99, doi: 10.1016/j.epsl.2017.07.039.

Mulholland, W. (1918), Earthquakes in their relation to the Los Angeles aqueduct, *Bulletin of the Seismological Society of America*, *8*, 13–19, doi: 10.1785/bssa0080010013.

Nevitt, J. M., B. A. Brooks, R. D. Catchings, M. R. Goldman, T. L. Ericksen, and C. L. Glennie (2020), Mechanics of near-field deformation during co- and post-seismic shallow fault slip, *Scientific reports*, *10*(1), 5031, doi: 10.1038/s41598-020-61400-9.

Nicholson, K., and M. Eley (1997), Geochemistry of manganese oxides: metal adsorption in freshwater and marine environments, *Geological Society special publication*, *119*(1), 309–326, doi: 10.1144/gsl.sp.1997.119.01.20.

Niemeijer, A., G. Di Toro, W. A. Griffith, A. Bistacchi, S. A. F. Smith, and S. Nielsen (2012), Inferring earthquake physics and chemistry using an integrated field and laboratory approach, *Journal of structural geology*, *39*, 2–36, doi: 10.1016/j.jsg.2012.02.018.

Niemeijer, A. R., C. Boulton, V. G. Toy, J. Townend, and R. Sutherland (2016), Large-displacement, hydrothermal frictional properties of DFDP-1 fault rocks, Alpine Fault, New Zealand: Implications for deep rupture propagation, *Journal of geophysical research. Solid earth*, *121*(2), 624–647, doi: 10.1002/2015JB012593.

Nourse, J. (2002), Middle Miocene reconstruction of the central and eastern San Gabriel Mountains, southern California, with implications for evolution of the San Gabriel fault and Los Angeles basin, *Geological Society of America Special Paper*, *365*, 161–185, doi: 10.1130/0-8137-2365-5.161.

O'Hara, K. (1992), Major- and trace-element constraints on the petrogenesis of a fault-related pseudotachylyte, western Blue Ridge province, North Carolina, *Tectonophysics*, *204*(3), 279–288, doi: 10.1016/0040-1951(92)90312-T.

Ostermeijer, G. A., F. M. Aben, T. M. Mitchell, T. K. Rockwell, M. Rempe, and K. Farrington (2022), Evolution of co-seismic off-fault damage towards pulverisation, *Earth and planetary science letters*, *579*(117353), 117,353, doi: 10.1016/j.epsl.2021.117353.

Powell, R. E. (1993), Chapter 1: Balanced palinspastic reconstruction of pre-late Cenozoic paleogeology, southern California: Geologic and kinematic constraints on evolution of the San Andreas fault system, *Geological Society of America Memoirs*, *178*, 1–106, doi: 10.1130/MEM178-P1.

Powell, R. E., and R. J. Weldon, II (1992), EVOLUTION OF THE SAN ANDREAS FAULT, *Annual Review of Earth and Planetary Sciences*, *20*(Volume 20, 1992), 431–468, doi: 10.1146/annurev.ea.20.050192.002243.

Renard, F., B. Cordonnier, D. K. Dysthe, E. Boller, P. Tafforeau, and A. Rack (2016), A deformation rig for synchrotron microtomography studies of geomaterials under conditions down to 10 km depth in the Earth, *Journal of synchrotron radiation*, *23*(Pt 4), 1030–1034, doi: 10.1107/S1600577516008730.

Rice, J. R., and S. T. Tse (1986), Dynamic motion of a single degree of freedom system following a rate and state dependent friction law, *Journal of geophysical research*, *91*(B1), 521–530, doi: 10.1029/jb091ib01p00521.

Richard, J., J.-P. Gratier, M.-L. Doan, A.-M. Boullier, and F. Renard (2014), Rock and mineral transformations in a fault zone leading to permanent creep: Interactions between brittle and viscous mechanisms in the San Andreas Fault, *Journal of geophysical research. Solid earth*, *119*(11), 8132–8153, doi: 10.1002/2014jb011489.

Rollinson, H. R., H. Rollinson, and V. Pease (2021), *Using Geochemical Data: To Understand Geological Processes*, Cambridge University Press.

Ross, D. C. (1984), *Possible Correlations of basement rocks across the San Andreas, San Gregorio-Hosgri, and Rinconada-Reliz-King City Faults*, U.S. Geological Survey Professional Paper, California.

Roten, D., K. B. Olsen, and S. M. Day (2017), Off-fault deformations and shallow slip deficit from dynamic rupture simulations with fault zone plasticity, *Geophysical research letters*, *44*(15), 7733–7742, doi: 10.1002/2017gl074323.

Rowe, C. D., and W. A. Griffith (2015), Do faults preserve a record of seismic slip: A second opinion, *Journal of structural geology*, *78*, 1–26, doi: 10.1016/j.jsg.2015.06.006.

Rumbiak, U., L. C-K., R. Al Furqan, M. Rosana, E. Yuningsih, B. Tsikouras, E. Ifandi, A. I. Malik, and H. Chen (2021), Geology, alteration geochemistry, and exploration geochemical mapping of the Ertsberg Cu-Au-Mo district in Papua, *Indonesia, Journal of Geochemical Exploration*, *232*.

Scharer, K., and A. Streig (2019), The San Andreas fault system: Complexities along a major transform fault system and relation to earthquake hazards, in *Transform Plate Boundaries and Fracture Zones*, edited by J. C. Duarte, pp. 249–269, Elsevier, doi: 10.1016/b978-0-12-812064-4.00010-4.

Schleicher, A. M., S. N. Tourscher, B. A. Pluijm, and L. N. Warr (2009), Constraints on mineralization, fluid-rock interaction, and mass transfer during faulting at 2–3 km depth from the SAFOD drill hole, *Journal of Geophysical Research, [Solid Earth]*, *114, B04202*, doi: 10.1029/2008JB006092.

Scholz, C. H. (2019), *The Mechanics of Earthquakes and Faulting*, 3rd ed., 493 pp., Cambridge University Press.

Schulz, S. E., and J. P. Evans (1998), Spatial variability in microscopic deformation and composition of the Punchbowl fault, southern California: implications for mechanisms, fluid–rock interaction, and fault morphology, *Tectonophysics*, *295*(1-2), 223–244, doi: 10.1016/s0040-1951(98)00122-x.

Schulz, S. E., and J. P. Evans (2000), Mesoscopic structure of the Punchbowl Fault, Southern California and the geologic and geophysical structure of active strike-slip faults, *Journal of structural geology*, *22*(7), 913–930, doi: 10.1016/s0191-8141(00)00019-5.

Scott, C., J. Champenois, Y. Klinger, E. Nissen, T. Maruyama, T. Chiba, and R. Arrowsmith (2019), The 2016 M7 Kumamoto, Japan, earthquake slip field derived from a joint inversion of differential lidar topography, optical correlation, and InSAR surface displacements, *Geophysical research letters*, *46*(12), 6341–6351, doi: 10.1029/2019gl082202.

Shipton, Z. K. E., J. P. Abercrombie, R.e., and E. E. Brodsky (2006), The missing sinks: slip localization in, in *Earthquakes: Radiated Energy and the Physics of Faulting*, edited by R. Abercrombie, A. McGarr, G. Toro, and

H. Kanamori, p. 217–222, American Geophysical Union Monograph, Washington, DC.

Shreedharan, S., D. Saffer, L. M. Wallace, and C. Williams (2023), Ultralow frictional healing explains recurring slow slip events, *Science (New York, N.Y.)*, *379*(6633), 712–717, doi: 10.1126/science.adf4930.

Silver, L. T., and E. W. James (1988), Geologic setting and lithologic column of the Cajon Pass Deep Drillhole, *Geophysical research letters*, *15*(9), 941–944, doi: 10.1029/gl015i009p00941.

Smith, S. A. F., A. Bistacchi, T. M. Mitchell, S. Mittempergher, and G. Di Toro (2013), The structure of an exhumed intraplate seismogenic fault in crystalline basement, *Tectonophysics*, *599*, 29–44, doi: 10.1016/j.tecto.2013.03.031.

Spotila, J. A., M. A. House, A. E. Blythe, N. A. Niemi, and G. C. Bank (2002), Controls on the erosion and geomorphic evolution of the San Bernardino and San Gabriel Mountains, southern California, in *Contributions to Crustal Evolution of the Southwestern United States*, edited by A. Barthh, pp. 205–230,, Geological Society of America, southern California, doi: 10.1130/0-8137-2365-5.205.

Studnicky, C. (2021), Constraining Deformation Mechanisms of Fault Damage Zones: A Case Study of the Shallow San Andreas Fault at Elizabeth Lake, Southern California, Ph.D. thesis, Utah State University, Utah, USA.

Sutherland, M., J. R. Keaton, and C. Heron (2013), Correlating surface geology with 1913-vintage as-built geology across the San Andreas fault for seismic enhancement of the Elizabeth Tunnel, Los Angeles Aqueduct, *Geological Society of America. Programs with Abstracts*, *45*(6), 23.

Tayyebi, A., J. Telling, K. Hudnut, C. G. Davis, and C. (2017), *100 Years of accumulated deformation at depth observed in the Elizabeth Lake Tunnel*, Abstract G43C-04, American Geophysical Union Fall Meeting Abstracts, southern San Andreas Fault.

Tenthorey, E., and S. F. Cox (2006), Cohesive strengthening of fault zones during the interseismic period: An experimental study, *Journal of Geophysical Research: Solid Earth*, *111*(B9), doi: 10.1029/2005JB004122.

Townend, J. (2017), Petrophysical, geochemical, and hydrological evidence for extensive fracture-mediated fluid and heat transport in the Alpine Fault's hanging-wall damage zone, *Geochemistry, Geophysics, Geosystems*, *18*, 4709–4732, doi: 10.1002/2017GC007202.

Turcotte, D., P. Tag, and R. Cooper (1980), A steady state model for the distribution of stress and temperature on the San Andreas Fault, *Journal of geophysical research*, *85*, 6224–6230, doi: 10.1029/JB085IB11P06224.

Utada, M. (2001), Zeolites in Burial Diagenesis and Low-grade Metamorphic rocks, *Reviews in mineralogy and geochemistry*, *45*(1), 277–304, doi: 10.2138/rmg.2001.45.9.

Wallace, R. E. (1949), Structure of a portion of the San Andreas rift in southern California, *Geological Society of America bulletin*, *60*(4), 781, doi: 10.1130/0016-7606(1949)60[781:soapot]2.0.co;2.

Webb, S. M. (2011), The MicroAnalysis Toolkit: X-ray Fluorescence Image Processing Software, Amer, *Insti Phys. Conf*, p. 196–199, doi: 10.1063/1.3625338.

Wechsler, N., E. E. Allen, T. K. Rockwell, G. Girty, J. S. Chester, and Y. Ben-Zion (2011), Characterization of pulverized granitoids in a shallow core along the San Andreas Fault, Littlerock, CA, *Geophysical journal international*, *186*(2), 401–417, doi: 10.1111/j.1365-246x.2011.05059.x.

Weisenberger, T., and K. Bucher (2010), Zeolites in fissures of granites and gneisses of the Central Alps, *Journal of metamorphic geology*, *28*(8), 825–847, doi: 10.1111/j.1525-1314.2010.00895.x.

Wibberley, C., G. Yielding, and G. Di Toro (2008), Recent advances in the understanding of fault zone internal structure: a review, *Geological Society of London Special Publication*, *299*, 33–35, doi: 10.1144/SP299.2.

Williams, R. T., C. D. Rowe, K. Okamoto, H. M. Savage, and E. Eves (2021), How fault rocks form and evolve in the shallow San Andreas fault, *Geochemistry, geophysics, geosystems: G(3)*, *22*(11), 2021 010,092, doi: 10.1029/2021gc010092.

Xu, X., X. Tong, D. T. Sandwell, C. W. D. Milliner, J. F. Dolan, J. Hollingsworth, S. Leprince, and F. Ayoub (2016), Refining the shallow slip deficit, *Geophysical journal international*, *204*(3), 1843–1862, doi: 10.1093/gji/ggv563.

Yerkes, R. F., and R. H. Campbell (2005), Preliminary Geologic Map of the Los Angeles 30' x 60' Quadrangle, Southern California.

Zhao, D., C. Qu, R. Bürgmann, and X. Shan (2024), Characterizing Deep, Shallow, and Surface Fault Zone Deformation of the 2021 Mw 7.4 Maduo, China, Earthquake, *Seismological Research Letters*, *95*(1), 277–287, doi: 10.1785/0220230115.

Zielke, O., J. R. Arrowsmith, L. G. Ludwig, and S. O. Akciz (2010), Slip in the 1857 and Earlier Large Earthquakes Along the Carrizo Plain, *San Andreas Fault: Science*, *327*, 1119–1122,, doi: 10.1126/science.1182781.